Geophysical Journal International

Geophys. J. Int. (2017) **208,** 1592–1610
Advance Access publication 2016 December 9
GJI Geodynamics and tectonics

doi: 10.1093/gji/ggw462

The 2008 Methoni earthquake sequence: the relationship between the earthquake cycle on the subduction interface and coastal uplift in SW Greece

Andy Howell,[1] Kirill Palamartchouk,[2] Xanthos Papanikolaou,[3] Demitris Paradissis,[3] Costas Raptakis,[3] Alex Copley,[1] Philip England[4] and James Jackson[1]

[1]*COMET, Department of Earth Sciences, University of Cambridge, Bullard Labs, Madingley Road, Cambridge* CB3 0EZ, *United Kingdom.*
E-mail: arh79@cam.ac.uk
[2]*School of Civil Engineering and Geosciences, Newcastle University, Newcastle upon Tyne* NE1 7RU, *United Kingdom*
[3]*Higher Geodesy Laboratory, National Technical University,* GR-15780 *Athens, Greece*
[4]*Department of Earth Sciences, University of Oxford, South Parks Road, Oxford* OX1 3AN, *United Kingdom*

Accepted 2016 December 6. Received 2016 December 1; in original form 2016 September 1

SUMMARY

Seismological, GPS and historical data suggest that most of the 40 mm yr^{-1} convergence at the Hellenic Subduction Zone is accommodated through aseismic creep, with earthquakes of $M_W \lesssim 7$ rupturing isolated locked patches of the subduction interface. The size and location of these locked patches are poorly constrained despite their importance for assessment of seismic hazard. We present continuous GPS time-series covering the 2008 M_W 6.9 Methoni earthquake, the largest earthquake on the subduction interface since 1960. Post-seismic displacements from this earthquake at onshore GPS sites are comparable in magnitude with the coseismic displacements; elastic-dislocation modelling shows that they are consistent with afterslip on the subduction interface, suggesting that much of this part of the interface is able to slip aseismically and is not locked and accumulating elastic strain. In the Hellenic and other subduction zones, the relationship between earthquakes on the subduction interface and observed long-term coastal uplift is poorly understood. We use cGPS-measured coseismic offsets and seismological body-waveform modelling to constrain centroid locations and depths for the 2008 Methoni M_W 6.9 and 2013 Crete M_W 6.5 earthquakes, showing that the subduction interface reaches the base of the seismogenic layer SW of the coast of Greece. These earthquakes caused subsidence of the coast in regions where the presence of Pliocene–Quaternary marine terraces indicates recent uplift, so we conclude that deformation associated with the earthquake cycle on the subduction interface is not the dominant control on vertical motions of the coastline. It is likely that minor uplift on a short length scale (∼15 km) occurs in the footwalls of normal faults. We suggest, however, that most of the observed Plio-Quaternary coastal uplift in SW Greece is the result of thickening of the overriding crust of the Aegean by reverse faulting or distributed shortening in the accretionary wedge, by underplating of sediment of the Mediterranean seafloor, or a combination of these mechanisms.

Key words: Seismic cycle; Transient deformation; Subduction zone processes; Tectonics and landscape evolution.

1 INTRODUCTION

The Hellenic Subduction Zone, which borders the southern Aegean Sea between W Greece and SW Turkey (Fig. 1), accommodates convergence between the Nubian plate to the south and the deforming Aegean Sea to the north. GPS measurements and global plate models indicate that this convergence occurs at 40 mm yr^{-1} (e.g. Reilinger *et al.* 2006; Nocquet 2012). It is assumed that most of the convergence takes place by slip on a subduction interface dipping gently N–NE towards the Aegean (e.g. Caputo *et al.* 1970; McKenzie 1978; Ganas & Parsons 2009; Shaw & Jackson 2010).

Earthquakes with fault-plane solutions consistent with slip on a subduction interface are known in this region, typically with $M_W \lesssim 7$ and at depths up to 45 km (Taymaz *et al.* 1990; Benetatos *et al.* 2004; Shaw & Jackson 2010, this study). However, there has been insufficient earthquake activity over the past 2000 yr to account for the seismic moment release that would be required if all the slip on the interface were to take place seismically (Jackson

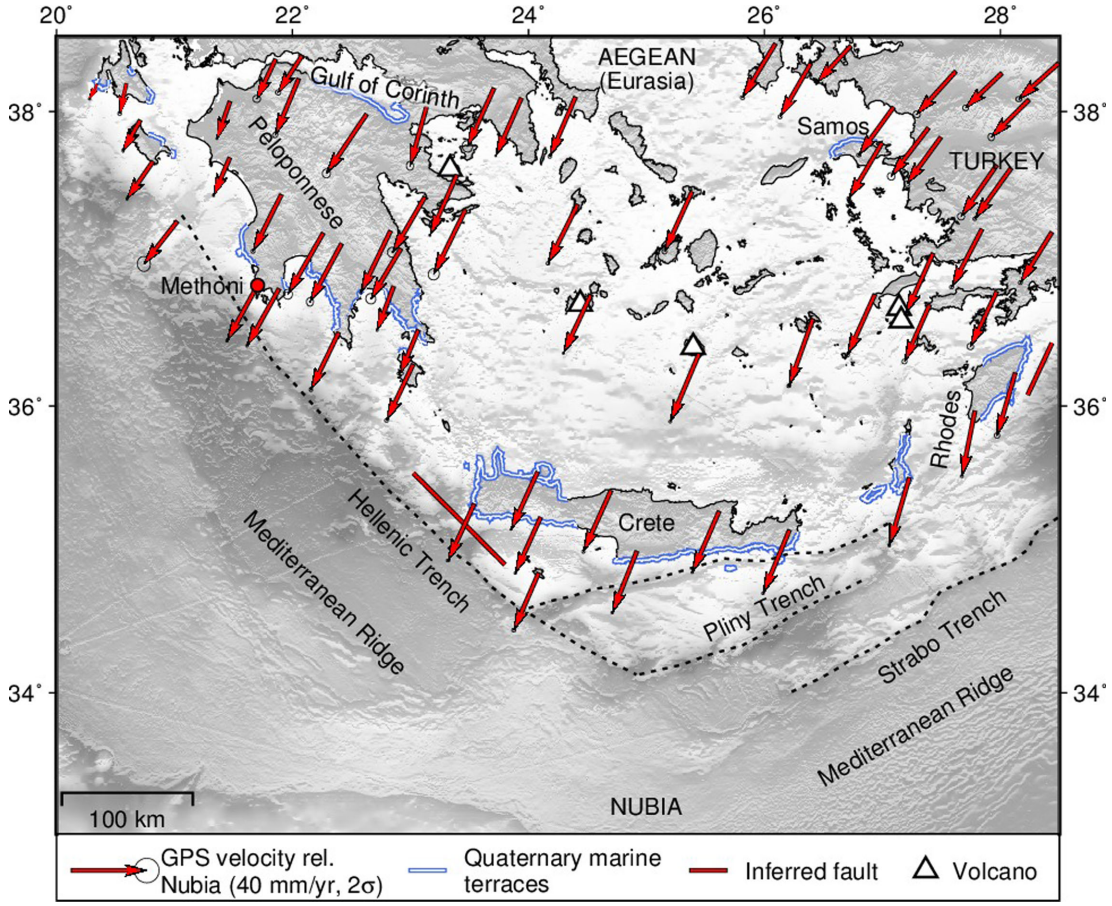

Figure 1. Selected GPS velocities and tectonic features in the Hellenic Subduction Zone. Coasts where uplift of Pliocene–Quaternary marine terraces has been observed are marked in white and blue, GPS velocities relative to stable Nubia are shown by red arrows and active volcanoes are marked by white triangles. The tsunamigenic reverse faults inferred by Shaw *et al.* (2008) and Howell *et al.* (2015) to explain uplift of Crete and Rhodes in large earthquakes are marked by thick red lines. Terrace locations are compiled from Kelletat *et al.* (1976), Gauthier (1979), Angelier (1979b), Peters *et al.* (1985), Armijo *et al.* (1996), Zelilidis *et al.* (1998), Stiros *et al.* (2000), Kontogianni *et al.* (2002), Gaki-Papanastassiou *et al.* (2009, 2011), Karymbalis *et al.* (2013), Gallen *et al.* (2014) and our own fieldwork. GPS velocities are from the data of Nocquet (2012) and this study, rotated into a Nubia-fixed reference frame using the pole of Reilinger *et al.* (2006). Volcanoes are from Siebert & Simkin (2002). Topography is SRTM15 (Becker *et al.* 2009; Sandwell *et al.* 2014).

& McKenzie 1988; Ambraseys 2009). GPS measurements also indicate absence of the elastic strain accumulation that would occur within the overriding Aegean material if the subduction interface was fully locked (Reilinger *et al.* 2006; Vernant *et al.* 2014). The earthquakes of $M_W \lesssim 7$ are therefore likely to occur on relatively small locked patches (smaller than 30 km × 30 km) on this otherwise predominantly aseismically slipping interface (e.g. Lay 2015).

A paradoxical feature of the Hellenic Subduction Zone is that at least two great ($M_W \geq 8.0$) historical earthquakes took place there (in AD 365 and AD 1303; Ambraseys 2009), which must have involved considerably larger fault dimensions than the earthquakes of $M_W \lesssim 7$ of modern times. While insufficient to account for the necessary seismic moment release if the subduction interface were entirely seismogenic, these earthquakes pose a puzzle in that we would not expect a single interface to be predominantly aseismic and also to move in occasional great earthquakes (which also produce large tsunamis; e.g. Ambraseys & Synolakis 2010; Stiros 2010).

One resolution of this puzzle is that the rare great earthquakes occur on separate reverse faults above the subduction interface within the overriding Aegean crust (e.g. Shaw *et al.* 2008; England *et al.* 2015). This interpretation also explains the presence of the Hellenic Trench System (Le Pichon *et al.* 1979; Huchon *et al.* 1982), which comprises several steep bathymetric escarpments within the Aegean lithosphere: the Hellenic Trench (or Matapan Trench; Mascle & Le Quellec 1980), Pliny Trench and Strabo Trench, which are shown in Fig. 1. These escarpments (up to 5 km in relief; Fig. 2a) are not trenches in the plate-tectonic sense: reflection seismic (Chaumillon & Mascle 1997; Huguen *et al.* 2001, 2006), wide-aperture seismic (Bohnhoff *et al.* 2001), gravity (Makris *et al.* 2013) and earthquake seismological data (Taymaz *et al.* 1990; Benetatos *et al.* 2004; Shaw & Jackson 2010) all show that the subduction interface projects to the surface at the Mediterranean Ridge (Fig. 1), where it is covered by ≥10 km of sediment.

The presence of reverse faults within the Aegean crust that project to the surface in the Hellenic Trench System can account for both the presence of these bathymetric escarpments and the occurrence of infrequent great earthquakes in a predominantly aseismic subduction zone. Slip on faults of this type is also able to fit the spatial distribution of uplifted Holocene palæoshorelines on Crete (e.g. Pirazzoli *et al.* 1982; Shaw *et al.* 2008) and Rhodes (Kontogianni *et al.* 2002; Howell *et al.* 2015) better than slip on a deeper subduction interface. Shaw *et al.* (2008) used radiocarbon dating and elastic-dislocation modelling to show that Holocene uplift in SW Crete (up to 9 m) is consistent with uplift in a single earthquake on a 30°-dipping reverse fault that projects to the surface in the Hellenic Trench (Fig. 1), probably the destructive AD 365 earthquake. Some

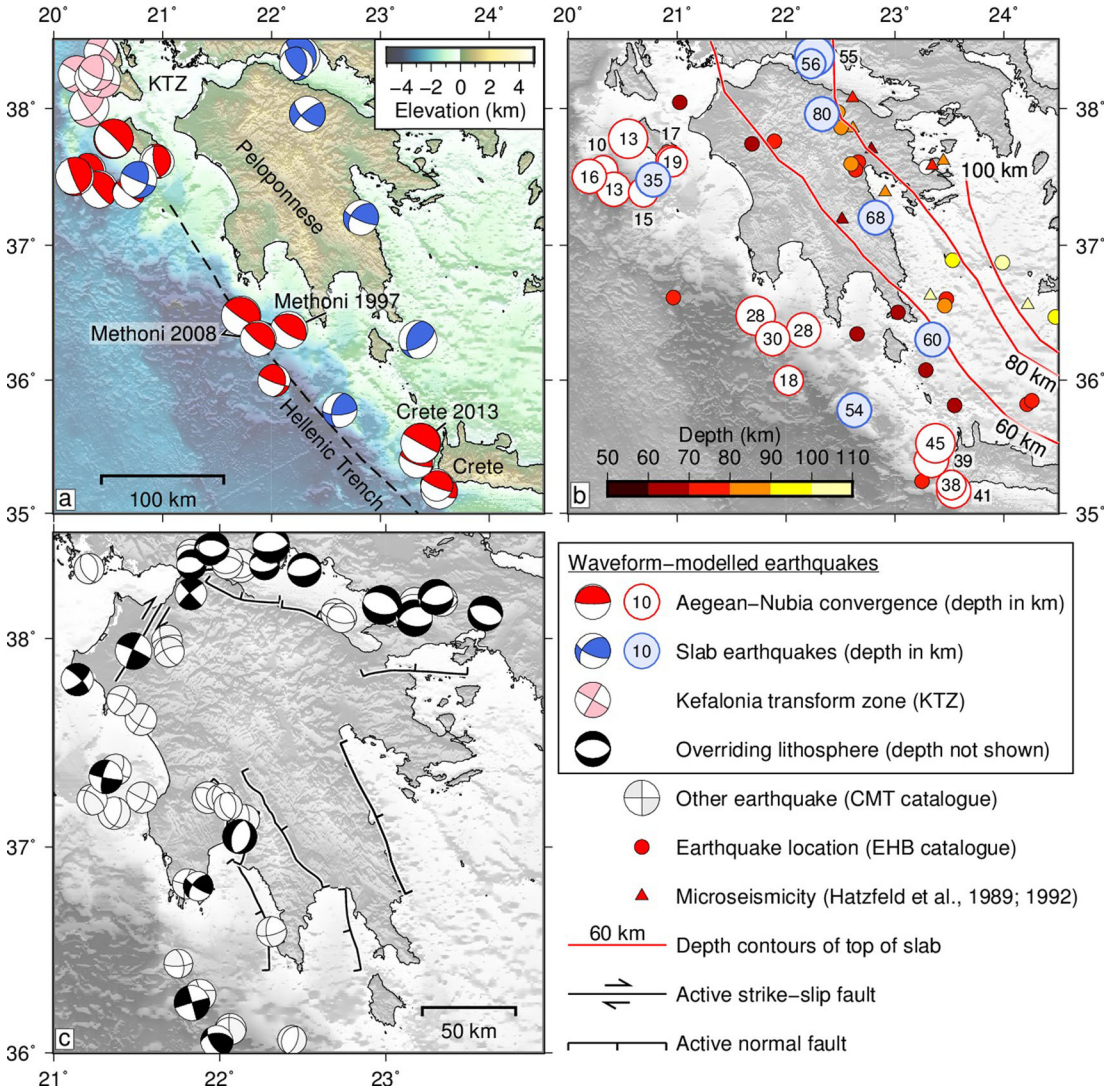

Figure 2. Overview of the seismicity of the W Hellenic Subduction Zone. (a) Mechanisms of waveform-modelled earthquakes on the subduction interface between the Aegean and Nubia (red) and in the downgoing Nubian plate (blue). Strike-slip earthquakes in the Kefalonia Transform Zone (KTZ) are marked in pink. 'Methoni 1997' and 'Crete 2013' show some earthquakes discussed in the text. (b) Depths (in km) corresponding to the earthquakes on the subduction interface and in the downgoing plate in (a), with the circles coloured according to their classification in (a). Earthquake locations from the EHB catalogue (Engdahl *et al.* 1998; International Seismological Centre 2016) are marked by coloured circles according to depth, while earthquakes located by Hatzfeld *et al.* (1989) and Hatzfeld (1994) are marked by triangles. Red lines show approximate contours of the top of the subduction interface. (c) Mechanisms of waveform-modelled earthquakes within the overriding lithosphere (black) and other earthquakes from the CMT catalogue, with some known major normal and strike-slip faults mapped from field and seismic-reflection data. Fault traces are schematic and modified from Caputo *et al.* (2013) and waveform-modelled earthquakes are from Kiratzi (2003), Benetatos *et al.* (2004), Shaw & Jackson (2010) and this study.

authors have suggested that the AD 365 event was a normal-faulting earthquake (e.g. Wegmann 2008), but we consider this unlikely, as we discuss in Section 5.2 and Appendix B.

Uplifted Holocene and Pliocene–Quaternary shorelines are observed along many of the coastlines of Greece close to the Hellenic Trench System (Fig. 1; e.g. Kelletat *et al.* 1976; Gauthier 1979; Angelier *et al.* 1982; Pirazzoli *et al.* 1982), and their presence has been attributed to a variety of mechanisms (e.g. Shaw *et al.* 2008; Gaki-Papanastassiou *et al.* 2009; Caputo *et al.* 2010; Gallen *et al.* 2014; Strobl *et al.* 2014). It is important for the assessment of earthquake and tsunami hazard in the eastern Mediterranean to determine: (1) how the earthquake cycle on the Aegean–Nubia subduction interface relates to these observed vertical motions of the coastline of southern Greece, and (2) how much of the observed coastal uplift is related to faulting of the type inferred to explain uplift of Crete and Rhodes.

This study presents time-series from continuous GPS (cGPS) stations in the SW Peloponnese (SW Greece; Figs 1 and 2a) over the period 2004–2015, focussing on the M_W 6.9 Methoni earthquake of 2008 February 14, which was one of the largest earthquakes in SW Greece since 1960 (Anderson & Jackson 1987; Shaw & Jackson 2010). We compare the observed coseismic displacements from this event and its aftershocks with those predicted from seismological source models and show that this earthquake is likely to have been on the subduction interface. We show that the post-seismic deformation from the Methoni earthquake sequence is also consistent with afterslip on the same interface. We then show that neither coseismic slip nor post-seismic deformation associated with

earthquakes on the subduction interface like the Methoni events is able to produce the observed long-term (Pliocene–Quaternary) uplift of their adjacent coasts. We conclude that the observed vertical motions of the coast are probably related to faulting or ductile shortening within the overriding Aegean lithosphere rather than slip on the subduction interface itself.

2 THE 2008 METHONI EARTHQUAKE SEQUENCE

This study covers the part of the plate boundary zone shown in Fig. 2(a), from W Crete in the east to the SW side of the Peloponnese. The Hellenic Trench is present along the whole of this section of the plate boundary, and the presence of Pliocene–Quaternary marine terraces close to the coast of the three peninsulas in the S Peloponnese (Kelletat *et al.* 1976; Fig. 1) shows that, like Crete, this area is being uplifted. Inland, internal deformation of the Peloponnese observed using GPS data is minimal (Davies *et al.* 1997; Clarke *et al.* 1998; Briole *et al.* 2000; Floyd *et al.* 2010), but there are active normal faults striking at a high angle to the subduction zone (Armijo *et al.* 1992; Papanikolaou *et al.* 2007; Mason *et al.* 2015; Fig. 2c), with slip rates of up to 2 mm yr^{-1} (Benedetti *et al.* 2002). Strike-slip earthquakes in the NW coastal region of the Peloponnese appear to be related to faulting in the Kefalonia Transform Zone (Kahle *et al.* 1993; Louvari *et al.* 1999; Shaw & Jackson 2010; Karakostas *et al.* 2015). Data from seismic receiver functions (Pearce *et al.* 2012; Sachpazi *et al.* 2015), microseismicity (Hatzfeld *et al.* 1989; Hatzfeld 1994) and body-waveform modelling of earthquake focal mechanisms and depths (e.g. Taymaz *et al.* 1990; Benetatos *et al.* 2004; Shaw & Jackson 2010) show that the subduction interface dips shallowly (∼10°) under the Peloponnese and Crete, before steepening under the Gulf of Corinth and the volcanic arc. Earthquakes also occur within the subducting slab to depths of ∼100 km, probably including the 1903 M_W ∼ 7.7-8.1 Kythira earthquake, which occurred somewhere in the region S of the Peloponnese; little is known about this event but it is generally thought to have occurred within the downgoing plate (Kárník 1971; Engdahl & Villaseñor 2002; Konstantinou *et al.* 2006). Depth contours for the subduction interface are shown in Fig. 2(b).

The February 2008 Methoni earthquake sequence began at 10:09 UTC on February 14 with an M_W 6.9 reverse-faulting earthquake at 28 km depth (M1, Fig. 3; centroid depths and mechanisms are from body-waveform modelling unless specified; Shaw & Jackson 2010; Roumelioti *et al.* 2009). It was followed 2 hr later by a M_W 6.3 event at 12:08 (M2), at 30 km depth, and on February 20 by an M_W 6.1 strike-slip earthquake (M3) at 12 km depth (within the overriding lithosphere; Shaw & Jackson 2010). Seismicity in the area south of the February 14 events stayed consistently high for the next four months: gCMT moment tensors for 12 events of $4.8 \leq M_W < 6.0$ between February and June 2008 are shown in Fig. 3 (M4–15; Ekström *et al.* 2012). Also in June 2008, the Achaia-Elia (or Movri; A1) earthquake occurred in the western Peloponnese at ∼20 km depth (Shaw & Jackson 2010), but does not appear to have ruptured the surface (e.g. Ganas *et al.* 2009; Stiros *et al.* 2013; Serpetsidaki *et al.* 2014). Durand *et al.* (2014) suggest that earthquakes with $M_W \geq 5.0$ in Greece during 2008 followed an approximately SW–NE progression related to the spread of seismicity following an earthquake in the downgoing Nubian lithosphere on 2008 January 6 (L1, Fig. 3). We now present new cGPS data that illuminate the coseismic and post-seismic deformation associated with this earthquake sequence.

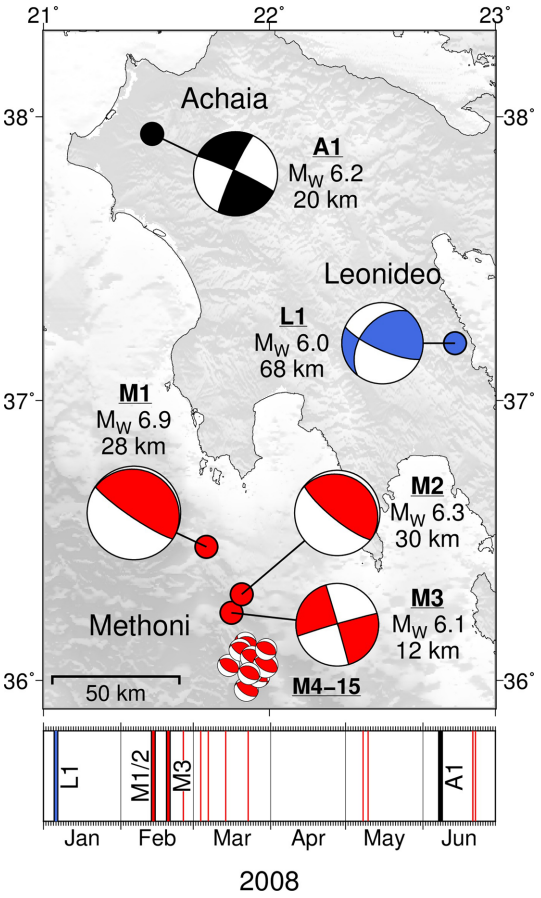

Figure 3. Locations and timings of earthquakes in 2008 referred to in the text. The upper panel shows the locations of the earthquakes, their magnitudes, centroid depths and the labels by which they are referred to in the text (underlined). The lower panel shows the dates of the earthquakes, colour-coded so that events match the top panel. M4–15 are the 12 small reverse-faulting events that occurred in the 6 months after the Methoni earthquakes in the area to their S.

3 GPS DATA AND TREATMENT

The main data presented in this study are the time-series from the cGPS stations shown in Fig. 4(a). Most of these data were collected between 2000 and 2015 as part of a joint project between the Higher Geodesy Laboratory of the National Observatory of Athens and Oxford University, though we also use some stations from the Corinth Rift Observatory (e.g. Bernard *et al.* 2014, https://gpscope.dt.insu.cnrs.fr/chantiers/corinthe/). Many of the cGPS stations were installed in 2011–2013, so the data available for analysis of the 2008 earthquakes are restricted to those stations marked in red in Fig. 4(a).

The processing of raw GPS data used GIPSY-OASIS II software (v. 6.4), Precise Point Positioning strategy (Zumberge *et al.* 1997) and precise non-fiducial orbits and clocks (product version 2.1) from JPL. The daily solutions were then converted to ITRF2008 using transformation parameters from JPL. In daily session processing we estimated station positions and clocks, tropospheric delays and their horizontal gradients for 30 hr sessions, centred at the midday of each day. The VMF-1 mapping function was used to model tropospheric delay (Boehm *et al.* 2006), and zenith wet delay and the horizontal tropospheric gradients were modelled as Random Walk variables with variance of 8 and 0.8 mm hr$^{-1/2}$, respectively. Earth and ocean

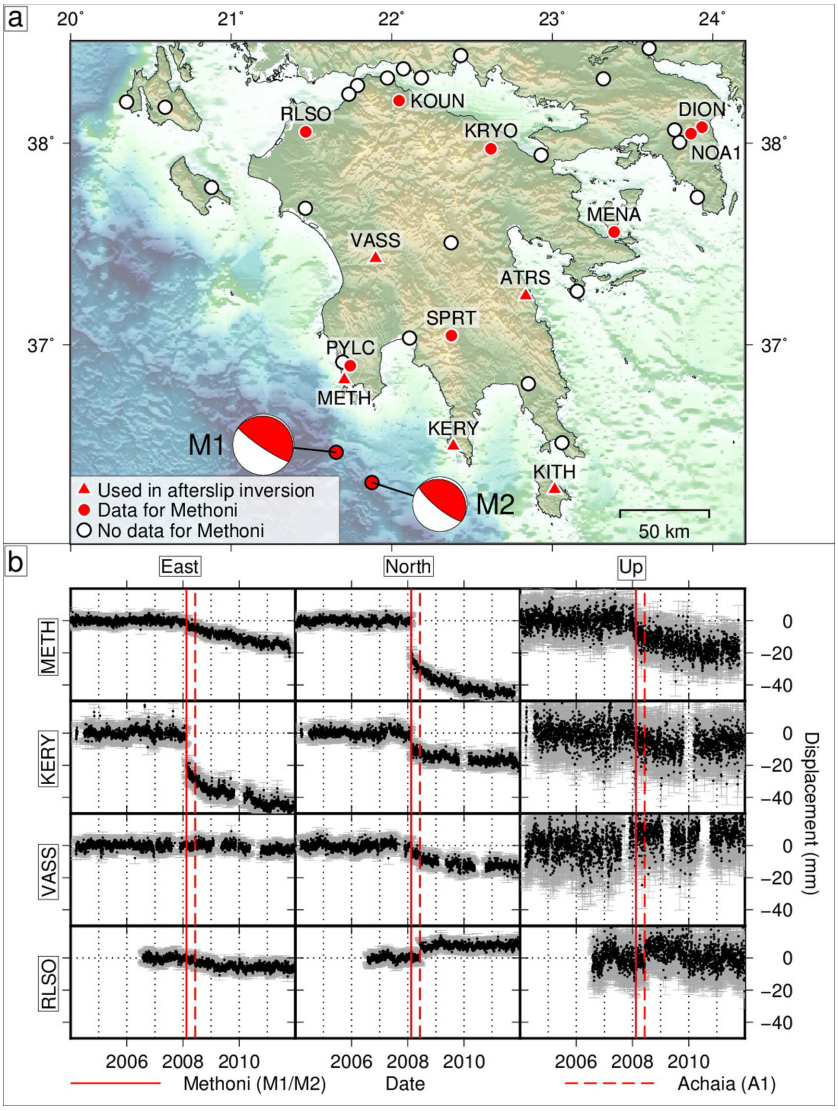

Figure 4. (a) cGPS stations in southern and central Greece. Stations with and without time-series data for 2008 February 14 are marked by red and white circles respectively. Stations used in our afterslip inversion are marked by red triangles (all stations marked by triangles have time-series with data coverage for the Methoni earthquakes). The 2008 February 14 M_W 6.9 (left) and 6.3 (right) earthquakes are also plotted. Topography is from SRTM15 (Becker *et al.* 2009). (b) Detrended time-series for selected stations. All are treated using the method discussed in the text and illustrated in the supplementary material. Grey bars show 2σ errors. The dates of the 2008 February 14 Methoni and June 6 Achaia earthquakes are marked by solid and dashed red lines.

tides were predicted using the TPXO7.2 model (Egbert *et al.* 2010) and atmospheric loading effects were taken into account following Tregoning & van Dam (2005). Absolute calibrations for satellite and receiver antenna phase-centre variations and offsets were used according to Schmid *et al.* (2007). Integer phase ambiguities were fixed using the wide-lane phase-bias product from JPL (Bertiger *et al.* 2010).

Time-series were processed using CATS software (Williams 2008), which was also used to remove seasonal variations (annual and semi-annual terms in the time-series). Data were then rotated from IRTF2008 into the Eurasia-fixed reference frame provided by Altamimi *et al.* (2011). We are principally interested in departures from the long-term (interseismic) velocities at these sites, so detrend the time-series using pre-2008 data, assuming the velocity to have been constant from the beginning of the time-series until immediately before the earthquake. Formal errors for the time-series are unrealistically small, so we take the standard deviation of the detrended pre-2008 data as a more realistic estimate of error, except for the few cases where the estimated formal error is larger than the standard deviation. Final, detrended time-series for selected stations (with realistic uncertainties) are shown in Fig. 4(b). These clearly show that at the stations closest to the Methoni (M1 and M2) earthquakes the coseismic (marked by red lines) and post-seismic offsets (the curved transient offsets after the earthquakes) are of similar magnitude.

4 METHODS AND ANALYSIS

4.1 Coseismic displacements: methods

Our first aim is to compare the observed coseismic displacements at our GPS sites with displacements predicted from seismological estimates of earthquake source parameters. We use the waveform-modelled sources of Shaw & Jackson (2010), re-assessing them to obtain the reliable estimates of error in seismologically

Table 1. Source parameters and their uncertainties for selected waveform-modelled earthquakes discussed in the text. Latitude and longitude are from the EHB catalogue (Engdahl *et al.* 1998), except for the 2013 Crete event (for which the hypocentre is from the ISC) and the 2008 February 14 Methoni earthquakes, for which our relocated hypocentres are plotted (see the text and Fig. 6 for details). M_W is calculated using the method of Hanks & Kanamori (1979).

Date	Location	Longitude (°)	Latitude (°)	Centroid depth (km)	Strike (°)	Dip (°)	Slip vector (°)	M_W
1997-10-13	Methoni	22.161	36.374	28+4/−10	310	17+6/−10	209 ± 10	6.4
2008-02-14	Methoni (M1)	21.664	36.344	28 ± 6	310	8+10/−8	215 ± 10	6.9
2008-02-14	Methoni (M2)	22.044	36.353	30+4/−6	310	15+/−12	217 ± 12	6.3
2013-10-12	Crete	23.3718	35.5277	45 ± 4	315	12+8/−10	208 ± 8	6.5

determined source parameters listed in Table 1. The inversion procedure uses the MT5 program (Zwick *et al.* 1994) and the method of McCaffrey & Abers (1988) and McCaffrey *et al.* (1991). We deconvolve seismograms (from the IRIS DMC) from their instrument response and reconvolve them with the response of a WWSSN 15–100 s long-period seismometer. At these periods, earthquakes with $M_W \leq 7.0$ can be approximated as a point source, and the program uses a downhill inversion technique to find source parameters that minimize the least-squares misfit between observations and computed synthetic seismograms. This technique, the details of which are discussed extensively elsewhere (e.g. Maggi *et al.* 2000; Shaw & Jackson 2010; Craig *et al.* 2014), is effective for estimating earthquake centroid depths (accurate to about ±4 km; Molnar & Lyon-Caen 1989; Taymaz *et al.* 1991; Maggi *et al.* 2000) and also improves estimates of source parameters such as strike, dip and rake compared to the gCMT catalogue (Dziewonski *et al.* 1981; Ekström *et al.* 2012). The fit of synthetic to observed waveforms for our best-fitting source model for the M_W 6.9 Methoni (M1) earthquake is shown in Fig. 5.

We use the same velocity model as Shaw & Jackson (2010) because (1) this is reasonable given what is known of the upper crustal structure offshore (e.g. Chaumillon & Mascle 1997); and (2) it facilitates comparison with their other waveform-modelled earthquake sources. This velocity model consists of a layer of sediment 8 km thick (V_P 4.5 km s^{-1} and V_S 2.59 km s^{-1}) overlying a crustal layer (V_P of 6.5 km s^{-1} and V_S 3.75 km s^{-1}) which contains the earthquake, with a water layer of 1–4 km depth depending on the earthquake location. We estimate uncertainties by fixing the source parameter of interest at values away from the best-fit, re-inverting for all other parameters and comparing the misfit to the best-fit solution (see Molnar & Lyon-Caen 1989; Taymaz *et al.* 1990); best-fitting source parameters and uncertainties for earthquakes discussed in this study are listed in Table 1. We also re-assess the seismological source model for the 1997 October 13 M_W 6.4 earthquake which occurred close to the hypocentres of the 2008 Methoni earthquakes (Fig. 2a), using its depth to provide a further constraint on the depth of the subduction interface in this region.

The waveform-modelling technique treats earthquakes as point sources, but we are interested in the Methoni earthquakes as ruptures of fault patches. When modelling coseismic displacements at GPS stations, we therefore use the method of Okada (1985), treating the earthquakes as slip of a rectangular dislocation. Since the Methoni earthquakes are of modest size, we treat the earthquake sources as square dislocations, with the length of one side (L) estimated from the seismic moment using the empirical scaling relation $u = 5 \times 10^{-5} L$, where u is magnitude of slip (for earthquakes of the size of the Methoni events, these range between 0.5 and 2 m; Fig. 6; Scholz *et al.* 1986; Wells & Coppersmith 1994). Exact patch dimensions are not important, however: at the distances between the earthquakes and our stations, displacements are much more sensitive to the scalar seismic moment (patch area × slip) than to patch dimension alone.

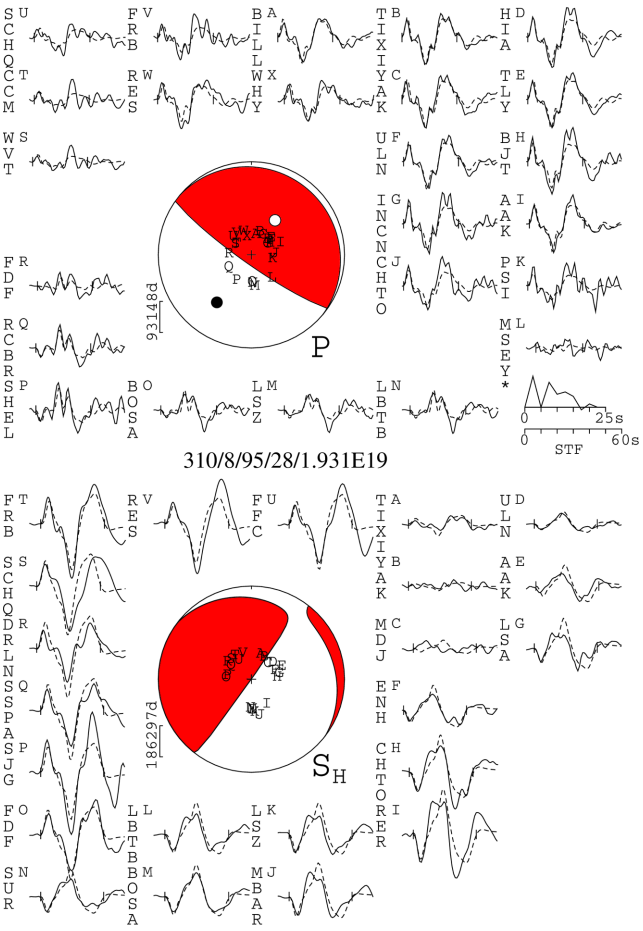

Figure 5. Fit of synthetic to observed waveforms for the 2008 February 14 Methoni M_W 6.9 earthquake. The event header (between the two focal spheres) shows the strike, dip, rake, centroid depth and scalar seismic moment (in Nm) of the minimum misfit solution. The top focal sphere shows the lower hemisphere stereographic projection of the *P*-waveform nodal planes, and the positions of the seismic stations used in the inversion. The lower panel shows the *SH* focal sphere. Capital letters next to the station codes correspond to the position on the focal sphere, ordered clockwise by azimuth, starting at north. Solid and dashed lines show the observed and synthetic waveforms respectively. The inversion window is marked by vertical lines on each waveform. The source-time function (STF) is shown, with the time scale for the waveforms below it. The amplitude scales for the waveforms are shown below each focal sphere. The P- and T-axes within the *P*-waveform focal sphere are shown by a solid and an open circle, respectively.

In order to test whether our GPS-measured coseismic displacements are consistent with the seismologically determined source parameters, we perform a grid search for the locations of the M_W 6.9 and M_W 6.3 reverse-faulting earthquake centroids (M1 and M2 in Fig. 3), varying latitude, longitude and depth in 1 km increments. Of the remaining six parameters required to define a single-patch

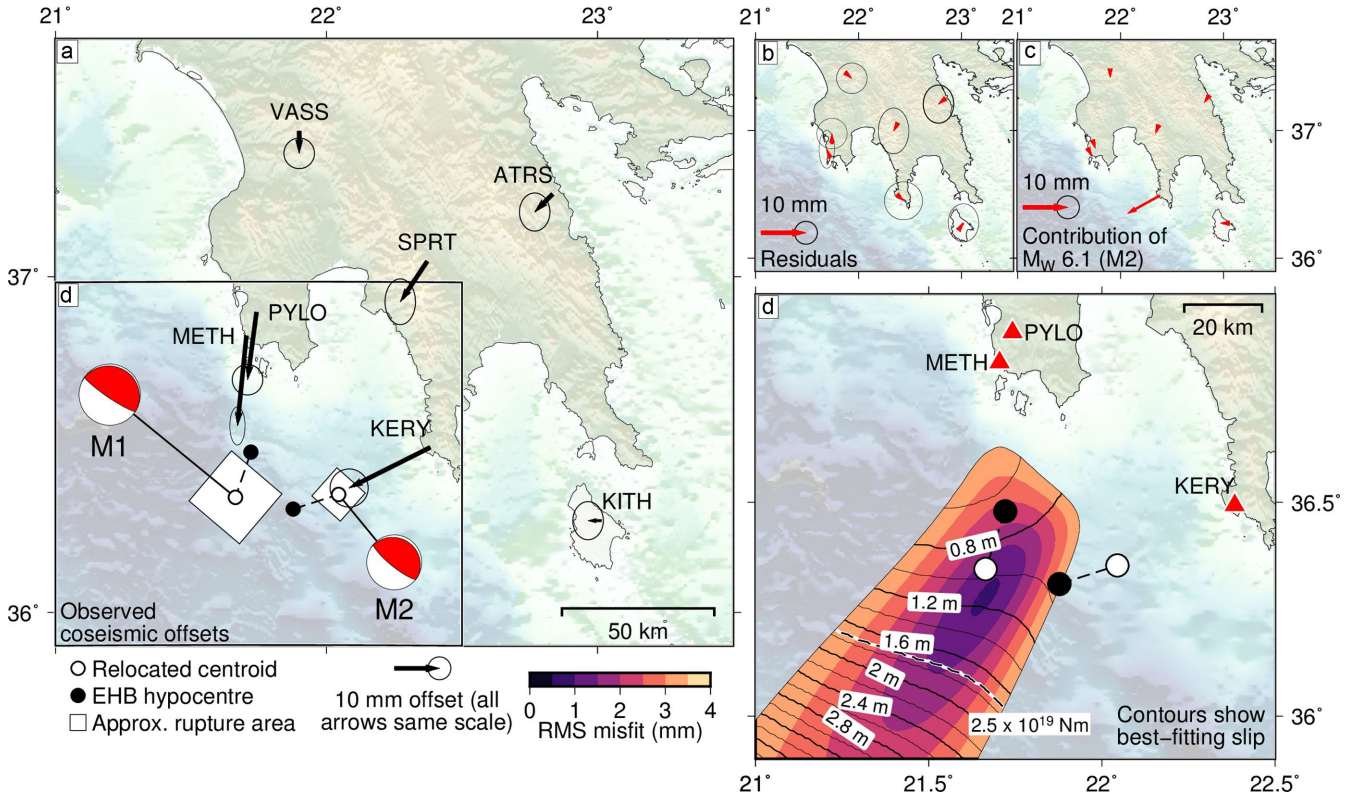

Figure 6. (a) Observed coseismic displacements, marked by black arrows with error ellipses. (b) Residual displacements from our best-fitting combined model for the M_W 6.9 and 6.3 (M1 and M2) earthquakes, with arrows at the same scale as in (a). (c) Contribution of the M_W 6.3 (M2) earthquake to the modelled earthquake, again at the same scale. (d) Coloured contours show variation of RMS misfit with centroid location of the M_W 6.9 (M1) event. Black lines show the amount of slip to achieve the best fit to the GPS data for that centroid location; they reveal the consequent trade-off between moment and centroid location. South of the dashed line, earthquake source models that fit the data predict a seismic moment $M_0 \geq 2.5 \times 10^{19}$ Nm, the maximum plausible seismic moment from our seismological inversions. The centroids and modelled rupture areas of both the M_W 6.9 and 6.3 models in (a) are shown by white circles and squares respectively and the EHB hypocentres for these events are shown in black. Station names are shown next to displacement arrows in (a) and their locations are marked by red triangles in (d).

Okada (1985) source, we fix the along-strike length and down-dip width at the value calculated using the scaling relation above, solve for slip using standard least-squares methods, and allow strike, dip and rake to vary by 1° increments. However, we discard source models whose slip vector is outside ±10° of the seismologically constrained values in Table 1.

4.2 Coseismic displacements: analysis

Fig. 6(a) shows the centroid locations for our best-fitting model of the two 2008 February 14 earthquakes, the EHB (Engdahl *et al.* 1998) hypocentres for these earthquakes reported by the ISC (International Seismological Centre 2016), the observed coseismic displacements and the residuals from comparison of the displacements predicted by our best-fitting source model with the observations. These results show that the coseismic displacements in our GPS time-series are consistent with earthquakes located within the likely error (±15 km) of the EHB hypocentres and with our seismologically determined source parameters.

There are trade-offs between location and other source parameters for both of these earthquakes. The largest, illustrated for the M_W 6.9 (M1) earthquake in Fig. 6(d), is between seismic moment and distance of the centroid from the coast and is not surprising since all of our stations (on land) lie to the NE of both earthquakes. Nonetheless, for the M_W 6.9 event, RMS misfit deteriorates rapidly if the model centroid is moved N of the EHB hypocentre, with individual misfits highest at PYLO and METH, the two stations with the largest and best-determined coseismic displacements. The earthquake may therefore have occurred significantly further from the coast, but its centroid cannot be more than 15 km N of the EHB hypocentre. The maximum distance of the earthquake centroid from the coast is poorly constrained by the GPS-measured coseismic offsets, but the predicted values of seismic moment for source models with centroids more than 40 km SW of the EHB hypocentre are too high to be consistent with our seismologically determined value of $1.93 \pm 0.5 \times 10^{19}$ Nm (black dashed line in Fig. 6d). The minimum distance from the coast of the earthquake centroid is constrained by the fit of the model to the observed GPS offsets rather than the seismic moment.

The smaller earthquake (M2) is also subject to a trade-off between distance from the coast and seismic moment, but its location is poorly constrained by the GPS data, with negligible displacements at all stations apart from KERY (Fig. 6c). In practice, the simplest approach is to find the location and source parameters for the M_W 6.9 earthquake that fit the observed GPS offsets best, and then to find source parameters for the smaller earthquake that minimize the residual at KERY. Some results of this approach are shown in Fig. 6, where the centroid of the smaller earthquake is ∼20 km from the EHB hypocentre, slightly larger than the largest mislocations for IASPEI test events in the EHB catalogue (Engdahl *et al.* 1998). However, a common trade-off between the

seismologically determined depth, seismic moment and source time function allows a shallower, larger (M_W 6.4) earthquake to produce the same displacement at KERY with its centroid nearer the EHB hypocentre.

We conclude that the observed GPS offsets are consistent with the seismological data, and that both earthquakes (M1 and M2) ruptured the subduction interface, which is well defined by the depths and mechanisms of numerous shallow-dipping thrusts along the SW side of the Peloponnese (Fig. 2; e.g. Shaw & Jackson 2010).

4.3 Post-seismic deformation: methods

Our second aim is to establish whether the observed post-seismic deformation can be explained as the effects of afterslip on the spatial continuation of the fault that ruptured coseismically, a phenomenon that has been observed in many subduction zones and for other reverse faults (e.g. Chlieh *et al.* 2007; Mahsas *et al.* 2008; Ozawa *et al.* 2011; Vigny *et al.* 2011; Thomas *et al.* 2014). Our inversion uses the PCAIM (principal components) software of Kositsky & Avouac (2010) and the detrended time-series from the stations marked by triangles in Fig. 4(a). Prior to inversion, static coseismic displacements associated with the 2008 February 20 Methoni (M3) and June 8 Achaia (A1) strike-slip earthquakes are removed from the time-series.

We use E and N components at five stations (METH, KERY, VASS, ATRS and KITH), but use vertical time-series only from METH and KERY, because the small magnitude and large errors on the vertical time-series at the other stations make it easy for other effects (for example, related to equipment changes) to be mistaken for tectonic displacements. Instead, we compare the observed vertical time-series at these stations with the modelled time-series predicted by our inversion using the other data, to check that the observed time-series at these stations are compatible with our results. We use the coseismic offsets measured at Pilos (PYLO) in our grid search in Section 4.1, but the station only became active in August 2007, so uncertainties in interseismic velocity are large and it is difficult to determine how quickly the velocity at the station returns to its interseismic value. We therefore do not use the time-series from PYLO in our afterslip inversion. We were unable to fit the time-series from Sparta (SPRT) and suspect that the site is affected by a local slope instability, so exclude it from the inversion. We assume that the post-seismic signals we model are entirely due to the Methoni earthquakes. The post-seismic deformation associated with the Achaia earthquake, the only other large earthquake in the vicinity in the relevant time interval, appears to be negligible at the stations closest to its hypocentre; these stations (RLSO and KOUN) are closer to the epicentre than the closest station we analyse (VASS) so this assumption seems reasonable.

We require our solution to be consistent with slip on the subduction interface. While there have been several seismological studies of the interface, their resolution offshore has been limited by an absence of stations (Pearce *et al.* 2012; Sachpazi *et al.* 2015; Kassaras *et al.* 2016), so that the geometry of the interface up-dip of the Methoni earthquakes is poorly constrained. In the absence of better constraints, we assume the subduction interface is planar, passing through our best-fitting centroid for the M_W 6.9 Methoni earthquake (M1) and dipping at 8° (the best-fitting dip from our seismological estimates). We vary the centroid location and dip within their uncertainties (listed in Table 1) to test the sensitivity of the inversion to these parameters, and also test the effect of different patch sizes on the results of the inversion. Finally, we assume that the magnitude of slip tends to zero away from the main slip area, so augment the penalty on slip at the sides and lower end of the fault model.

This choice of a simple geometry for our fault model means that we do not investigate the possibility of post-seismic slip on steeper faults above the subduction interface. Although afterslip on these steeper faults is observed elsewhere (e.g. Copley & Reynolds 2014), the dip and location of any such faults offshore from the Peloponnese are poorly constrained so we are unable to model them effectively. In the absence of better data we restrict our fault model to the simple geometry described above, accepting that at least some of the post-seismic deformation may occur on faults other than the subduction interface, particularly in regions further from the coast.

Our model extends down-dip to 45 km depth, which is the depth of the deepest waveform-modelled earthquakes on the subduction interface (Shaw & Jackson 2010, this study) and also of the deepest microseismicity on Crete (Meier *et al.* 2004). This is probably an overestimate of the depth extent of the seismogenic layer under the Peloponnese, since the Methoni earthquakes are the deepest moderate-sized earthquakes to have occurred there since 1960 (Shaw & Jackson 2010) and local microseismicity only reaches to 35 km depth (Papoulia & Makris 2004; Kassaras *et al.* 2016), but we use the more conservative of these depth estimates when setting limits for the extent of the model fault plane.

At its up-dip limit, the subduction interface may be buried by 10 km of sediment on the Nubian plate (e.g. Chaumillon & Mascle 1997; Huguen *et al.* 2001; Makris *et al.* 2013). We therefore carry out two sets of inversions to investigate whether it is possible to fit the observations with (1) fault slip that extends all the way to the surface and (2) slip on a subduction interface deeper than 10 km (an approximate thickness for the sediment).

The initial set-up of our model subduction interface allows the inversion to specify slip up to 150 km along strike from the centroid of the M_W 6.9 (M1) earthquake, relocated from the EHB hypocentre using the method in Section 4.1 and the observed coseismic GPS offsets. We experiment with different along-strike fault widths, as well as varying patch sizes, the value of the Laplacian smoothing weight, and the number of principal components.

4.4 Post-seismic deformation: analysis

Fig. 7(a) shows example results from an inversion for afterslip. Many slip distributions are able to fit the observed time-series to an acceptable level (reduced χ^2 goodness-of-fit $\leq$1.0) with one principal component of slip, an exponential relaxation time for all patches of 345 $\pm$ 51 days and a Laplacian smoothing weight of 10^4 or lower (Kositsky & Avouac 2010), but they all have two important features in common:

(i) **Most afterslip occurs on the offshore portions of the subduction interface**. This result is independent of patch size, smoothing and the extent of the fault model. However, this area is furthest from our stations, where resolution would be expected to be lowest. In order to test the resolving power of our network in the offshore regions, we use the method of Backus & Gilbert (1970) and Tarantola (2005) to calculate a resolution matrix **R** (shown in Fig. 7b), where

$$\mathbf{R} = \mathbf{G}^t(\mathbf{G}\mathbf{G}^t)^{-1}\mathbf{G} \quad (1)$$

and **G** is the matrix of Green's functions for the fault model. The elements of **R** are dimensionless numbers between 0 (no resolution) and 1 (full resolution) for each patch in the fault model. If there were no noise at our stations, an inversion would be expected to specify

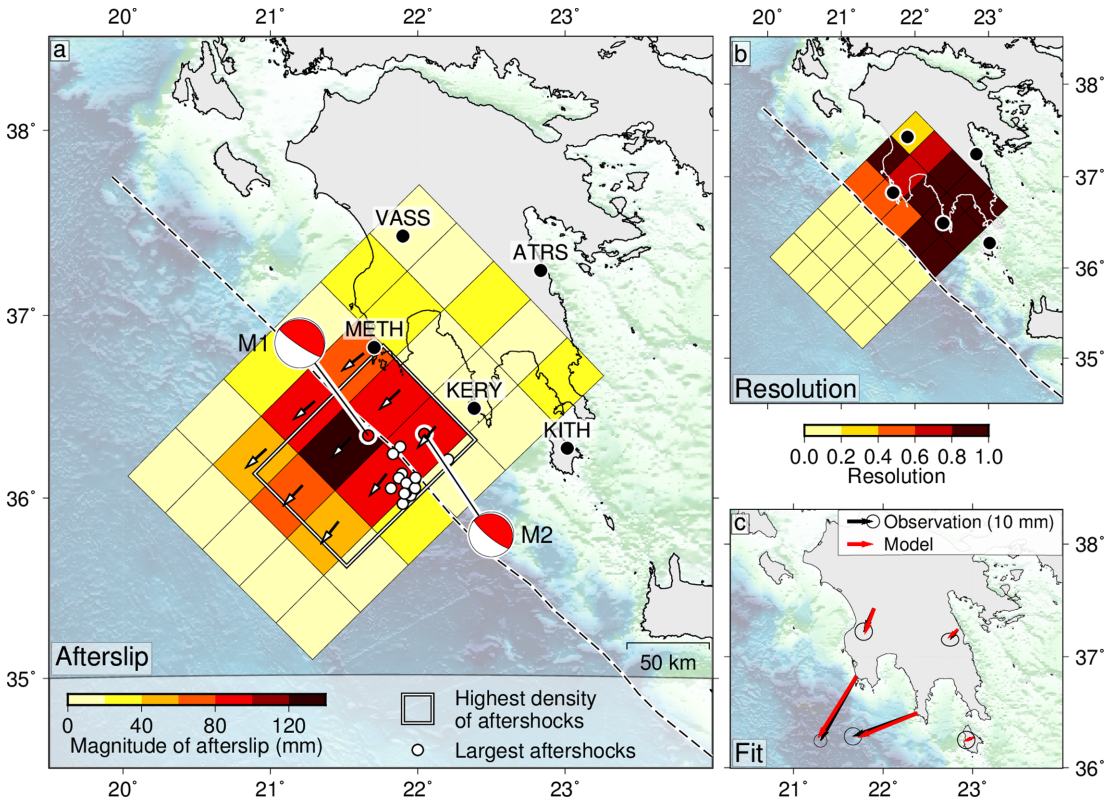

Figure 7. (a) Results of afterslip inversion of post-seismic GPS time-series using the PCAIM software of Kositsky & Avouac (2010). Slip was inverted for using one principal component and a value for the Laplacian smoothing operator of 10^4. The Methoni earthquakes (M1 and M2) are shown, the trace of the Hellenic Trench is marked by a dashed black line, and the stations used in the inversion are shown by black circles. Arrows show slip-vector directions for fault patches where the inversion predicts mean slip ≥50 mm and the white box shows the region with the highest spatial density of aftershocks (see Fig. 8). (b) The resolution matrix for the network and the model subduction interface shown in (a). (c) Fit of the model in (a) to cumulative displacements in the 3 yr following the Methoni earthquakes.

the slip on a patch with a resolution of 1 entirely correctly, and to be completely insensitive to slip on a patch with a resolution of 0. The resolution for our network is good (≥0.8) under the Peloponnese, but rapidly becomes poorer with distance offshore (Fig. 7b). The prediction of minimal afterslip NE of the coastline is therefore likely to be robust. Although the inversion specifies some small slip in a few patches under the Peloponnese, since we are able to fit the observed time-series to an acceptable level with a fault model where slip is restricted to be shallower than 35 km (Fig. A1), we conclude that slip under the Peloponnese is likely to be minor.

Offshore, resolution for our network is poor so the slip distribution around and up-dip of the coseismic ruptures is poorly constrained. Fig. 7(a) shows a plausible afterslip distribution for which afterslip is greatest in the region where elevated levels of seismicity were observed following the earthquake (Fig. 8), but due to a trade-off between magnitude of slip and distance from the coast we cannot determine the up-dip extent of afterslip. In many subduction zones the region closest to the trench is creeping, so the absence of seismicity there does not necessarily indicate an absence of near-trench slip (e.g. Hyndman *et al.* 1997; Lay 2015). Furthermore, reflection-seismic data show numerous folds in the sediments of the Mediterranean ridge (e.g. Huguen *et al.* 2001), so it is likely that much of the shortening in these sediments is accommodated inelastically and is therefore not observable using either seismological or on-shore GPS data.

(ii) **Post-seismic moment release is equivalent to or greater than coseismic moment release.** Despite the low sensitivity of our network to slip in the region up-dip of the coseismic ruptures, a trade-off between magnitude and areal extent of afterslip allows us to estimate a minimum value for the release of moment in the 3 yr following the earthquake. We run inversions with slip restricted from the surface down to a specified depth, which we vary. This reduces the area over which afterslip is allowed to occur, and allows us to test the robustness of the large slip area in our best inversion results. We are able to fit the data to an acceptable level (χ^2 goodness-of-fit ∼1.0) with slip restricted to be below 25 km, but fits to individual stations (most importantly METH and KERY) deteriorate significantly if slip is restricted to be deeper than this. When we reduce the area over which afterslip occurs, the mean slip over the remaining area increases greatly, so that even our most spatially restricted inversion requires a moment release of 4×10^{19} Nm (equivalent to M_W 7.1) to be able to match the magnitude of the post-seismic signal observed at our cGPS stations. This is not surprising given that the GPS-observed post-seismic and coseismic offsets at our stations are of roughly equal magnitude (both ∼20 mm at METH and KERY).

Some of the post-seismic deformation may be off-fault (rather than localized on the subduction interface), particularly since we do not model post-seismic viscous relaxation due to uncertainties in the viscosity structure for this area. The effects of viscous relaxation in the equivalent regions of other subduction zones are generally small in magnitude compared to coseismic displacements (e.g. Perfettini *et al.* 2005), so its contribution to our time-series is likely to be unimportant. The release of seismic moment from afterslip is likely

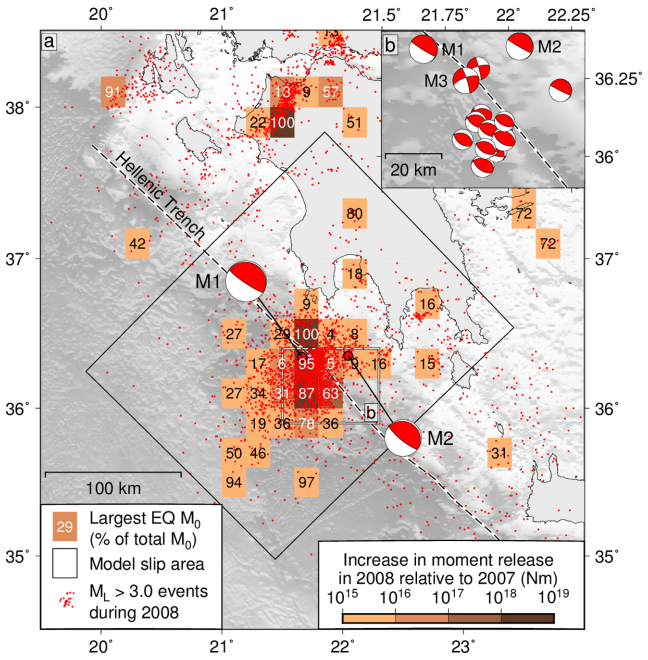

Figure 8. (a) Changes in seismicity in the NOA earthquake catalogue (D'Alessandro *et al.* 2011) from 2007 to 2008. Filled rectangles show areas where total seismic moment release in 2008 in a 0.1° × 0.1° area is greater than the total moment release in 2007 in the same area by at least 10^{15} Nm (equivalent to M_W 4.0). Red dots show locations of earthquakes with $M_L \geq 3.0$. Numbers in boxes show the fraction of the total seismic moment accounted for by the single largest earthquake in that 0.1° × 0.1° region as a percentage. The black line marks the edge of the fault model shown in Fig. 7(a). The dashed line marks the trace of the Hellenic Trench. Mechanisms of the Methoni earthquakes (M1 and M2) are shown in red. (b) Mechanisms and relative locations of the Methoni earthquakes (M1–3) and their aftershocks.

to be slightly lower than that predicted by our models, but we conclude that afterslip following the Methoni earthquakes is likely to have been widespread, releasing a seismic moment that was comparable to or greater than the coseismic moment release. Post-seismic deformation of comparable magnitude to the coseismic deformation has been observed for other faults (most notably following the 2004 Parkfield earthquake, around which much of the San Andreas fault is creeping; Barbot *et al.* 2009; Thomas *et al.* 2014); it is consistent with widespread aseismic slip in the areas around the rupture, and in the case of the Hellenic subduction zone may indicate that interseismic strain close to the subduction interface represents a small fraction of the convergence rate between Nubia and the lithosphere of the Aegean.

5 DISCUSSION

5.1 Locking of the subduction interface

Our analysis of the distribution of afterslip (Section 4.4 and Fig. 7a) suggests that it was spread over a relatively large area around the earthquake ruptures and therefore that large areas of the subduction interface are not locked, consistent with previous analyses of seismic and GPS data (Jackson & McKenzie 1988; Vernant *et al.* 2014) and with the suggestion of Shaw & Jackson (2010) that earthquakes on the interface may rupture isolated locked patches, as has been observed for other subduction zones (e.g. Lay 2015).

The relationship between coseismic rupture and interseismic or post-seismic creep is a complex one, with suggestions that creeping patches can also rupture coseismically through dynamic weakening (e.g. Noda & Lapusta 2013). However, our results are consistent with a large part of the subduction interface undergoing post-seismic creep. The results of our inversions suggest that most of the afterslip to the Methoni earthquake was on the offshore part of the subduction interface.

Seismological data provide some evidence of seismic slip in the region SW of the 2008 February 14 (M1 and M2) earthquakes: there were 12 reverse-faulting events of $M_W \geq 4.8$ in the area south of the M1 and M2 events in the 4 months following the Methoni earthquakes (Figs 3 and 8b), and there is an increase in seismicity in 2008 relative to 2007 in much of the area up-dip of the Methoni earthquakes, accompanied by a significant increase in the rate of release of seismic moment (Fig. 8). It is possible that at least some of this increased seismic activity is related to slip on the up-dip parts of the subduction interface. For many of the 0.1° × 0.1° bins in Fig. 8, the largest earthquake during the period of interest accounts for only a small fraction of the total moment release, which is consistent with gradual release of seismic moment in the months following the M1 and M2 earthquakes. Seismicity rates remain low in the shallowest 10–20 km of the subduction interface throughout 2008, but this is the area where in many subduction zones deformation is thought to be predominantly aseismic or inelastic (e.g. Hill *et al.* 2012; Lay 2015), so an absence of seismicity in this area does not necessarily reflect an absence of deformation.

The cGPS and seismological data are therefore consistent with large-magnitude, widespread afterslip in the part of the subduction interface around the patches that ruptured in the Methoni earthquakes and therefore with a low degree of locking on much of the Aegean–Nubia subduction interface in this area.

5.2 Relationship between subduction and long-term coastal uplift

The locations of the Methoni earthquakes and of an M_W 6.5 event on the subduction interface near Crete in 2013 (Fig. 2a) allow us to address an unresolved problem of eastern Mediterranean tectonics: the mechanism responsible for coastal uplift of SW Greece. Pliocene–Quaternary marine terraces indicative of recent uplift are found on all of the islands above the Hellenic Trench System and in the Peloponnese (e.g. Kelletat *et al.* 1976; Angelier 1979a; Gauthier 1979; Pirazzoli *et al.* 1982, 1989; Gaki-Papanastassiou *et al.* 2009; Caputo *et al.* 2010; Gallen *et al.* 2014, see Fig. 1).

The terraces represent uplift on a length scale that is consistent with faulting of the elastic upper crust. We use the term uplift to mean upward motion relative to the geoid and assume that, because erosion rates in this area are low, rates of uplift of the land surface, of rocks, and of palæoshorelines are the same at a given location. The region containing these terraces is affected by four sets of active faults capable of changing surface heights: (i) normal faults whose strikes are approximately north–south and sub-perpendicular to the trench (e.g. Armijo *et al.* 1992; Gaki-Papanastassiou *et al.* 2009; Caputo *et al.* 2010); (ii) normal faults whose strikes are approximately east–west and sub-parallel to the trench (e.g. Caputo *et al.* 2010; Gallen *et al.* 2014); (iii) the subduction interface; (iv) reverse faults above the interface (e.g. Pirazzoli *et al.* 1996; Shaw *et al.* 2008; Mouslopoulou *et al.* 2015). Surface uplift may also result from distributed crustal thickening, either by underplating of sediment or by ductile deformation of the crust.

Uplift of the footwalls of normal faults is widely observed in the Aegean region (e.g. Armijo *et al.* 1992; Stiros *et al.* 2000; McNeill & Collier 2004; Gaki-Papanastassiou *et al.* 2009), but the hanging walls of these faults subside much more rapidly than the footwalls rise. The widespread uplift that is seen in Crete and the Peloponnese cannot, therefore, be explained by displacements on normal faults that strike sub-perpendicular to the trenches (e.g. Armijo *et al.* 1992; Gaki-Papanastassiou *et al.* 2009). Such displacements may nevertheless modulate uplift on a horizontal length scale comparable with the vertical extent of faulting [∼15 km, (e.g. Jackson *et al.* 1982; Lyon-Caen *et al.* 1988; Gaki-Papanastassiou *et al.* 2009)].

Wegmann (2008) and Gallen *et al.* (2014) argued that coastal uplift in the Hellenic Plate boundary zone may be attributed to a combination of sedimentary underplating and uplift of the footwalls of normal faults that strike sub-parallel to the plate boundary and dip oceanwards. Gallen *et al.* (2014) suggested that some of the trenches in the Hellenic Trench System are the bathymetric expression of such normal faults. Wegmann (2008) suggested that the AD 365 earthquake occurred on such a normal fault south of Crete and was responsible for the late-Holocene uplift of SW Crete. This suggestion is examined in Appendix B and shown to be implausible. One objection to the suggestion that AD 365 was a normal-faulting earthquake is that an extremely large magnitude of coseismic slip (tens to hundreds of metres) is required if the late-Holocene uplift of SW Crete is to be explained by normal faulting. Second, even if normal faulting were to penetrate as far down as the plate interface (∼45 km, or 3-to-4 times the maximum observed depth of normal-faulting earthquakes of the region; Lyon-Caen *et al.* 1988; Hatzfeld *et al.* 2000), the length scale of the uplift is much shorter than that observed. We conclude that the normal faults striking parallel to the trenches do not exert a primary control on the surface elevation of the region. Instead, following England *et al.* (2015), we suggest that they are an example of the well-understood phenomenon of parallel reverse and normal faulting, with the normal faulting being within crust of greater surface elevation and higher gravitational potential energy (e.g. Dalmayrac & Molnar 1981; Copley *et al.* 2009; Farías *et al.* 2011; Tsuji *et al.* 2013).

The mechanisms and depths of the 2008 Methoni M_W 6.9 (M1) and 2013 Crete earthquakes (source parameters in Table 1) place them on the subduction interface, so we use their locations to test the hypothesis that coastal uplift on Crete and in the Peloponnese relates to permanent deformation during the earthquake cycle on this interface. It has been suggested, particularly for the Andean subduction zone, that cumulative deformation (including uplift) of the overriding plate occurs coseismically during earthquakes on the subduction interface where there is some permanent component of deformation that is not recovered elastically during the interseismic period (e.g. Loveless *et al.* 2005; Baker *et al.* 2013; Wesson *et al.* 2015; Melnick 2016).

Our analysis in Section 4.1 shows that the minimum distance from the coast of the centroid of the Methoni M_W 6.9 earthquake (M1) is well constrained by GPS data; an earthquake source model with a centroid more than 15 km N of the EHB hypocentre does not fit the coseismic offsets observed in our GPS time-series to an acceptable level (Fig. 6d). The predicted distribution of vertical displacements from our northernmost plausible fault model (centroid in Fig. 6) is shown in Fig. 9(b), with coseismic and post-seismic *subsidence* at METH and KERY (as shown by the time-series in Fig. 4) and predicted subsidence everywhere onshore, in a region where the presence of marine terraces shows long-term uplift (the marine terrace at Koroni is illustrated in Fig. 9a). Of the earthquakes on the subduction interface since 1960, the Methoni M_W 6.9 event was one of the deepest and furthest NE, so it is likely to have ruptured close to the base of the seismogenic layer.

The same argument applies to the 2013 October 12 Crete earthquake (Fig. 9c), whose depth of 45 ± 5 km is close to the maximum depth of microseismicity in the region (Meier *et al.* 2004). As for the Methoni earthquakes, the distribution of vertical displacements estimated from our source model predicts *subsidence* onshore over almost all of W Crete (Fig. 9c), where the presence of marine notches and marine terraces shows that the coast has been uplifted during Quaternary time (Pirazzoli *et al.* 1982; Shaw & Jackson 2010). This result remains true even if the source model is translated 60 km SE along the strike of the subduction zone to simulate an earthquake at the same depth closer to the coast of Crete. Furthermore, Fig. 9(d) shows that if the fault plane for the 2013 earthquake is extrapolated along strike and up dip to 10 km depth, a model in which an earthquake takes place on the subduction interface does not predict uplift onshore; in fact, for this larger modelled earthquake, the boundary between predicted uplift and subsidence lies further SW than for the 2013 Crete earthquake. We conclude that both coseismic and post-seismic slip on the subduction interface are unlikely to be responsible for the coastal uplift, because the seismogenic part of the interface lies too far from the coast.

In contrast to the three mechanisms discussed so far, shortening and thickening of the overriding lithosphere can readily explain the coastal uplift. Displacements on a reverse fault cropping out close to the Hellenic Trench can explain both the distribution of late-Holocene palæoshorelines associated with the AD 365 earthquake and the Quaternary uplift of the surface of western Crete (Shaw *et al.* 2008, and Appendix B). A reverse fault dipping at 30°, rupturing to 40 km depth and reaching the surface in the Hellenic Trench is able to explain much of the spatial distribution of mapped terraces in the Peloponnese (Fig. 9e), and a more complex geometry of reverse faulting could explain the rest; the presence of a reverse fault of this type would have important implications for regional earthquake and tsunami hazard. Such a reverse fault would reach a depth of 15–20 km beneath the nearest coast, and would therefore be able to coexist with the less deeply penetrating onshore normal faults without the two types of fault intersecting (e.g. Lyon-Caen *et al.* 1988).

The widespread uplift recorded in the coastlines of the region may also result from underplating of sediment or from reverse faulting within, or ductile deformation of, the crust (Fig. 1; e.g. Angelier *et al.* 1982; Strobl *et al.* 2014). We relate crustal thickening to uplift by assuming isostatic compensation and crust and mantle densities of 2700 and 3300 kg m^{-3} respectively, for which 5.5 mm yr^{-1} of crustal thickening would cause 1 mm yr^{-1} of surface uplift. If this thickening were uniform over 100 km inland from the Hellenic Trench system, then each millimetre per year of uplift would require the underplating of 13 km of sediment at the present convergence rate of 40 mm yr^{-1}. Typical estimates of the rate of Plio-Quaternary uplift in these areas are generally lower than 1 mm yr^{-1} (e.g. Kelletat *et al.* 1976; Gauthier 1979; Gaki-Papanastassiou *et al.* 2009; Strobl *et al.* 2014) and the thickness of sediment offshore is at least 10 km (e.g. Chaumillon & Mascle 1997; Huguen *et al.* 2001), so if that thickness of sediment were all to be thrust beneath the Peloponnese, it would account for the observed uplift.

6 CONCLUSIONS

The 2008 February 14 M_W 6.9 Methoni earthquake occurred on the Eurasia–Nubia subduction interface SW of the Peloponnese.

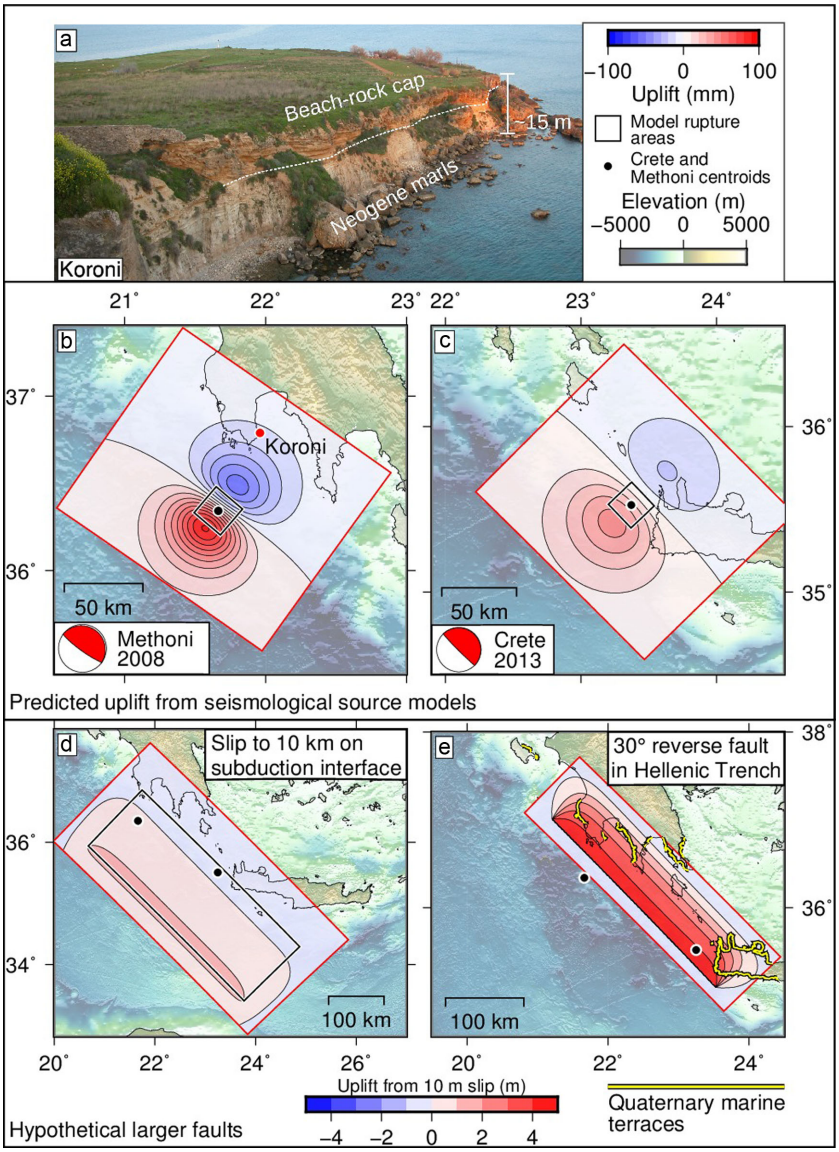

Figure 9. (a) Terrace with cap rock at Koroni, SW Peloponnese. (b) Modelled uplift distribution from our relocated seismological source model for the 2008 February 14 M_W 6.9 earthquake, with rupture area and centroid. Contours mark 10 mm intervals of uplift. (c) As for (b), but for the 2013 October 12 Crete earthquake. (d) Predicted uplift distribution for a 'megathrust earthquake' model, produced by extrapolating the fault plane for the 2013 Crete earthquake along-strike 200 km SE and NW from the centroid and updip to 10 km depth. Contours show uplift corresponding to 10 m slip on this fault model in 1 m intervals. (e) Predicted uplift distribution from a reverse fault above the subduction interface, from the surface (in the Hellenic Trench) to 45 km. Topography is from SRTM 15 (Becker *et al.* 2009; Sandwell *et al.* 2014) and marine terraces are from the same sources as Fig. 1.

Coseismic displacements measured with GPS are consistent with our best-fitting seismological source, which suggests a shallow-dipping thrust fault at 28 km depth. The post-seismic displacements in the 3 yr following the earthquake are most consistent with after-slip over a wide region around the coseismic rupture. Much of this part of the subduction interface appears to be able to creep, and is therefore probably not locked.

The 2008 Methoni earthquakes caused coseismic and post-seismic subsidence of regions in their hanging walls where the presence of Pliocene–Quaternary marine terraces indicates long-term uplift, and our source model for the 2013 Crete earthquake suggests that it also caused subsidence onshore. These earthquakes both occurred on the subduction interface at depths close to the lower limit of the seismogenic part of the subduction zone, so it is unlikely that deformation during the earthquake cycle on the subduction interface is responsible for observed Pliocene–Quaternary uplift. Instead, the widespread coastal uplift can be explained by thickening of the overriding crust either through distributed shortening or slip on reverse faults such as that thought to have generated the tsunamigenic AD 365 earthquake or some combination of these processes (e.g. Papadimitriou & Karakostas 2008; Shaw *et al.* 2008; Stiros 2010; Haghipour *et al.* 2012; Strobl *et al.* 2014).

ACKNOWLEDGEMENTS

AH is supported by a Shell Exploration studentship. This study forms part of the NERC- and ESRC-funded project 'Earthquakes

Without Frontiers' under grant NEJ02001X/1, and was partly funded by the NERC grant 'Looking inside the Continents from Space'. The figures were mostly produced using the Generic Mapping Tools (Wessel *et al.* 2013). NumPy, SciPy and ObsPy (Beyreuther *et al.* 2010) were used during data processing. We would like to thank the editor and reviewers for comments that improved the manuscript.

REFERENCES

Altamimi, Z., Collilieux, X. & Métivier, L., 2011. ITRF2008: an improved solution of the international terrestrial reference frame, *J. Geod.,* **85**(8), 457–473.

Ambraseys, N.N., 2009. *Earthquakes in the Mediterranean and Middle East: A Multidisciplinary Study of Seismicity up to 1900,* Cambridge Univ. Press.

Ambraseys, N. & Synolakis, C., 2010. Tsunami catalogs for the eastern Mediterranean, revisited, *J. Earthq. Eng.,* **14**(3), 309–330.

Anderson, H. & Jackson, J., 1987. Active tectonics of the Adriatic Region, *Geophys. J. Int.,* **91**(3), 937–983.

Angelier, J., 1979a. Recent Quaternary tectonics in the Hellenic Arc: examples of geological observations on land, *Tectonophysics,* **52**(1), 267–275.

Angelier, J., 1979b. *Néotectonique de l'arc Egéen,* Société Géologique du Nord.

Angelier, J., Lybéris, N., Le Pichon, X., Barrier, E. & Huchon, P., 1982. The tectonic development of the Hellenic Arc and the Sea of Crete: a synthesis, *Tectonophysics,* **86**(1–3), 159–196.

Armijo, R., Lyon-Caen, H. & Papanastassiou, D., 1992. East-west extension and Holocene normal-fault scarps in the Hellenic Arc, *Geology,* **20,** 491–494.

Armijo, R., Meyer, B., King, G.C.P., Rigo, A. & Papanastassiou, D., 1996. Quaternary evolution of the Corinth Rift and its implications for the Late Cenozoic evolution of the Aegean, *Geophys. J. Int.,* **126**(1), 11–53.

Backus, G. & Gilbert, F., 1970. Uniqueness in the inversion of inaccurate gross Earth data, *Phil. Trans. R. Soc. A,* **266**(1173), 123–192.

Baker, A., Allmendinger, R.W., Owen, L.A. & Rech, J.A., 2013. Permanent deformation caused by subduction earthquakes in northern Chile, *Nat. Geosci.,* **6**(6), 492–496.

Barbot, S., Fialko, Y. & Bock, Y., 2009. Postseismic deformation due to the M_W 6.0 2004 Parkfield earthquake: stress-driven creep on a fault with spatially variable rate-and-state friction parameters, *J. geophys. Res.,* **114**(B7), B07405, doi:10.1029/2008JB005748.

Becker, J.J. *et al.*, 2009. Global bathymetry and elevation data at 30 arc seconds resolution: SRTM30_PLUS, *Mar. Geod.,* **32**(4), 355–371.

Benedetti, L., Finkel, R., Papanastassiou, D., King, G., Armijo, R., Ryerson, F., Farber, D. & Flerit, F., 2002. Post-glacial slip history of the Sparta fault (Greece) determined by 36 Cl cosmogenic dating: evidence for non-periodic earthquakes, *Geophys. Res. Lett.,* **29**(8), 87–1–87–4.

Benetatos, C., Kiratzi, A., Papazachos, C. & Karakaisis, G., 2004. Focal mechanisms of shallow and intermediate depth earthquakes along the Hellenic Arc, *J. Geodyn.,* **37**(2), 253–296.

Bernard, P. *et al.*, 2014. The Corinth Rift Laboratory, Greece (CRL): a multidisciplinary near fault observatory (NFO) on a fast-rifting system, in *Am. Geophys. Union, Fall Meet. 2014,* Abstract #T12C-04.

Bertiger, W., Desai, S.D., Haines, B., Harvey, N., Moore, A.W., Owen, S. & Weiss, J.P., 2010. Single receiver phase ambiguity resolution with GPS data, *J. Geod.,* **84**(5), 327–337.

Beyreuther, M., Barsch, R., Krischer, L., Megies, T., Behr, Y. & Wassermann, J., 2010. ObsPy: a Python Toolbox for Seismology, *Seismol. Res. Lett.,* **81**(3), 530–533.

Boehm, J., Werl, B. & Schuh, H., 2006. Troposphere mapping functions for GPS and very long baseline interferometry from European Centre for Medium-Range Weather Forecasts operational analysis data, *J. geophys. Res.,* **111,** B02406, doi:10.1029/2005JB003629.

Bohnhoff, M., Makris, J., Papanikolaou, D. & Stavrakakis, G., 2001. Crustal investigation of the Hellenic subduction zone using wide aperture seismic data, *Tectonophysics,* **343**(3–4), 239–262.

Briole, P. *et al.*, 2000. Active deformation of the Corinth rift, Greece: results from repeated Global Positioning System surveys between 1990 and 1995, *J. geophys. Res.,* **105**(B11), 25 605–25 625.

Caputo, M., Panza, G.F. & Postpischl, D., 1970. Deep structure of the Mediterranean Basin, *J. geophys. Res.,* **75**(26), 4919–4923.

Caputo, R., Catalano, S., Monaco, C., Romagnoli, G., Tortorici, G. & Tortorici, L., 2010. Active faulting on the island of Crete (Greece), *Geophys. J. Int.,* **183**(1), 111–126.

Caputo, R., Caputo, R., Chatzipetros, A., Pavlides, S. & Sboras, S., 2013. The Greek Database of Seismogenic Sources (GreDaSS): state-of-the-art for northern Greece, *Ann. Geophys.,* **55**(5), doi:10.4401/ag-5168.

Chaumillon, E. & Mascle, J., 1997. From foreland to forearc domains: new multichannel seismic reflection survey of the Mediterranean Ridge accretionary complex (Eastern Mediterranean), *Mar. Geol.,* **138**(3), 237–259.

Chlieh, M. *et al.*, 2007. Coseismic slip and afterslip of the great M_W 9.15 Sumatra–Andaman earthquake of 2004, *Bull. seism. Soc. Am.,* **97**(1A), S152–S173.

Clarke, P.J. *et al.*, 1998. Crustal strain in central Greece from repeated GPS measurements in the interval 1989–1997, *Geophys. J. Int.,* **135**(1), 195–214.

Copley, A. & Reynolds, K., 2014. Imaging topographic growth by long-lived postseismic afterslip at Sefidabeh, east Iran, *Tectonics,* **33,** 330–345.

Copley, A., Boait, F., Hollingsworth, J., Jackson, J. & McKenzie, D., 2009. Subparallel thrust and normal faulting in Albania and the roles of gravitational potential energy and rheology contrasts in mountain belts, *J. geophys. Res.,* **114**(B5), B05407, doi:10.1029/2008JB005931.

Copley, A., Hollingsworth, J. & Bergman, E., 2012. Constraints on fault and lithosphere rheology from the coseismic slip and postseismic afterslip of the 2006 M_W 7.0 Mozambique earthquake, *J. geophys. Res.,* **117**(B3), doi:10.1029/2011JB008580.

Craig, T.J., Copley, A. & Jackson, J., 2014. A reassessment of outer-rise seismicity and its implications for the mechanics of oceanic lithosphere, *Geophys. J. Int.,* **197**(1), 63–89.

D'Alessandro, A., Papanastassiou, D. & Baskoutas, I., 2011. Hellenic Unified Seismological Network: an evaluation of its performance through SNES method, *Geophys. J. Int.,* **185**(3), 1417–1430.

Dalmayrac, B. & Molnar, P., 1981. Parallel thrust and normal faulting in Peru and constraints on the state of stress, *Earth planet. Sci. Lett.,* **55**(3), 473–481.

Davies, R., England, P., Parsons, B., Billiris, H., Paradissis, D. & Veis, G., 1997. Geodetic strain of Greece in the interval 1892–1992, *J. geophys. Res.,* **102**(B11), 24 571–24 588.

Durand, V., Bouchon, M., Floyd, M.A., Theodulidis, N., Marsan, D., Karabulut, H. & Schmittbuhl, J., 2014. Observation of the spread of slow deformation in Greece following the breakup of the slab, *Geophys. Res. Lett.,* **41**(20), 7129–7134.

Dziewonski, A.M., Chou, T.-A. & Woodhouse, J.H., 1981. Determination of earthquake source parameters from waveform data for studies of global and regional seismicity, *J. geophys. Res.,* **86,** 2825–2852.

Egbert, G.D., Erofeeva, S.Y. & Ray, R.D., 2010. Assimilation of altimetry data for nonlinear shallow-water tides: quarter-diurnal tides of the Northwest European Shelf, *Cont. Shelf Res.,* **30**(6), 668–679.

Ekström, G., Nettles, M. & Dziewoński, A., 2012. The global CMT project 2004–2010: centroid-moment tensors for 13,017 earthquakes, *Phys. Earth planet. Inter.,* **200–201,** 1–9.

Engdahl, E. & Villaseñor, A., 2002. Global seismicity: 1900–1999, *Int. Geophys.,* **81,** 665–690, cp1–cp2, doi:10.1016/S0074-6142(02)80244-3.

Engdahl, E.R., van der Hilst, R. & Buland, R., 1998. Global teleseismic earthquake relocation with improved travel times and procedures for depth determination, *Bull. seism. Soc. Am.,* **88,** 722–743.

England, P., Howell, A., Jackson, J. & Synolakis, C., 2015. Palæotsunamis and tsunami hazards in the Eastern Mediterranean, *Phil. Trans. R. Soc. A,* **373**(2053), 20140374, doi:10.1098/rsta.2014.0374.

Farías, M., Comte, D., Roecker, S., Carrizo, D. & Pardo, M., 2011. Crustal extensional faulting triggered by the 2010 Chilean earthquake: the Pichilemu seismic sequence, *Tectonics,* **30**(6), doi:10.1029/2011TC002888.

Floyd, M.A. *et al.*, 2010. A new velocity field for Greece: implications for the kinematics and dynamics of the Aegean, *J. geophys. Res.,* **115,** B10403, doi:10.1029/2009JB007040.

Gaki-Papanastassiou, K., Karymbalis, E., Papanastassiou, D. & Maroukian, H., 2009. Quaternary marine terraces as indicators of neotectonic activity of the Ierapetra normal fault, SE Crete (Greece), *Geomorphology,* **104**(1–2), 38–46.

Gaki-Papanastassiou, K., Maroukian, H. & Kourmpanian, V., 2011. The morphotectonic evolution of southern half of Kythira Island (Ionian sea, Greece) during the Quaternary, *Prace Geograficzne,* **127,** 49–59.

Gallen, S., Wegmann, K., Bohnenstiehl, D., Pazzaglia, F., Brandon, M. & Fassoulas, C., 2014. Active simultaneous uplift and margin-normal extension in a forearc high, Crete, Greece, *Earth planet. Sci. Lett.,* **398,** 11–24.

Ganas, A. & Parsons, T., 2009. Three-dimensional model of Hellenic Arc deformation and origin of the Cretan uplift, *J. geophys. Res.,* **114,** B06404, doi:10.1029/2008JB005599.

Ganas, A., Serpelloni, E., Drakatos, G., Kolligri, M., Adamis, I., Tsimi, C. & Batsi, E., 2009. The M_W 6.4 SW-Achaia (western Greece) earthquake of 8 June 2008: seismological, field, GPS observations, and stress modeling, *J. Earthq. Eng.,* **13**(8), 1101–1124.

Gauthier, A., 1979. Contribution à l'étude néotectonique du domaine Egéen: l'île de Rhodes (Dodécanèse, Grèce), *PhD thesis,* Academie de Versailles, Université de Paris XI, Centre d'Orsay.

Haghipour, N., Burg, J.-P., Kober, F., Zeilinger, G., Ivy-Ochs, S., Kubik, P.W. & Faridi, M., 2012. Rate of crustal shortening and non-Coulomb behaviour of an active accretionary wedge: the folded fluvial terraces in Makran (SE, Iran), *Earth planet. Sci. Lett.,* **355,** 187–198.

Hanks, T.C. & Kanamori, H., 1979. A moment magnitude scale, *J. geophys. Res.,* **84**(B5), 2348–2350.

Hatzfeld, D., 1994. On the shape of the subducting slab beneath the Peloponnese, Greece, *Geophys. Res. Lett.,* **21**(3), 173–176.

Hatzfeld, D. *et al.*, 1989. The Hellenic subduction beneath the Peloponnesus: first results of a microearthquake study, *Earth planet. Sci. Lett.,* **93**(2), 283–291.

Hatzfeld, D., Karakostas, V., Ziazia, M., Kassaras, I., Papadimitriou, E., Makropoulos, K., Voulgaris, N. & Papaioannou, C., 2000. Microseismicity and faulting geometry in the Gulf of Corinth (Greece), *Geophys. J. Int.,* **141**(2), 438–456.

Hill, E.M. *et al.*, 2012. The 2010 M_W 7.8 Mentawai earthquake: very shallow source of a rare tsunami earthquake determined from tsunami field survey and near-field GPS data, *J. geophys. Res.,* **117,** B06402, doi:10.1029/2012JB009159.

Howell, A., Jackson, J., England, P., Higham, T. & Synolakis, C., 2015. Late Holocene uplift of Rhodes, Greece: evidence for a large tsunamigenic earthquake and the implications for the tectonics of the eastern Hellenic Trench System, *Geophys. J. Int.,* **203**(1), 459–474.

Huchon, P., Lybéris, N., Angelier, J., Le Pichon, X. & Renard, V., 1982. Tectonics of the Hellenic Trench: a synthesis of sea-beam and submersible observations, *Tectonophysics,* **86**(1–3), 69–112.

Huguen, C., Mascle, J., Chaumillon, E., Woodside, J.M., Benkhelil, J., Kopf, A. & Volkonskaïa, A., 2001. Deformational styles of the eastern Mediterranean Ridge and surroundings from combined swath mapping and seismic reflection profiling, *Tectonophysics,* **343**(1), 21–47.

Huguen, C., Chamot-Rooke, N., Loubrieu, B. & Mascle, J., 2006. Morphology of a pre-collisional, salt-bearing, accretionary complex: the Mediterranean Ridge (eastern Mediterranean), *Mar. Geophys. Res.,* **27**(1), 61–75.

Hyndman, R.D., Yamano, M. & Oleskevich, D.A., 1997. The seismogenic zone of subduction thrust faults, *Isl. Arc,* **6**(3), 244–260.

International Seismological Centre, 2016. On-line Bulletin. International Seismological Centre, Thatcham, United Kingdom, http://www.isc.ac.uk.

Jackson, J. & McKenzie, D., 1988. The relationship between plate motions and seismic moment tensors, and the rates of active deformation in the Mediterranean and Middle East, *Geophys. J.,* **93,** 45–73.

Jackson, J., Gagnepain, J., Houseman, G., King, G., Papadimitriou, P., Soufleris, C. & Virieux, J., 1982. Seismicity, normal faulting, and the geomorphological development of the Gulf of Corinth (Greece): the Corinth earthquakes of February and March 1981, *Earth planet. Sci. Lett.,* **57**(2), 377–397.

Kahle, H.-G., Müller, M.V., Mueller, S. & Veis, G., 1993. The Kephalonia Transform Fault and the rotation of the Apulian Platform: evidence from satellite geodesy, *Geophys. Res. Lett.,* **20**(8), 651–654.

Karakostas, V., Papadimitriou, E., Mesimeri, M., Gkarlaouni, C. & Paradisopoulou, P., 2015. The 2014 Kefalonia Doublet (M_W 6.1 and M_W 6.0), Central Ionian Islands, Greece: seismotectonic implications along the Kefalonia Transform Fault Zone, *Acta Geophys.,* **63**(1), 1–16.

Kárník, V., 1971. *Seismicity of the European Area,* Springer.

Karymbalis, E., Papanastassiou, D., Gaki-Papanastassiou, K., Tsanakas, K. & Maroukian, H., 2013. Geomorphological study of Cephalonia Island, Ionian Sea, Western Greece, *J. Maps,* **9**(1), 121–134.

Kassaras, I., Kapetanidis, V. & Karakonstantis, A., 2016. On the spatial distribution of seismicity and the 3D tectonic stress field in western Greece, *Phys. Chem. Earth,* **95,** 50–72.

Kelletat, D., Kowalczyk, G., Schröder, B. & Winter, K.-P., 1976. A synoptic view on the neotectonic development of the Peloponnesian coastal regions, *Zeitschrift der Dtsch. Geol. Gesellschaft,* **127,** 447–465.

Kiratzi, A., 2003. Focal mechanisms of shallow earthquakes in the Aegean Sea and the surrounding lands determined by waveform modelling: a new database, *J. Geodyn.,* **36**(1–2), 251–274.

Kokinou, E. & Kamberis, E., 2009. The structure of the Kythira-Antikythira strait, offshore SW Greece (35.7°–36.6°N), *Geol. Soc. London, Spec. Publ.,* **311**(1), 343–360.

Konstantinou, K.I., Kalogeras, I.S., Melis, N.S., Kourouzidis, M.C. & Stavrakakis, G.N., 2006. The 8 January 2006 earthquake (M_w 6.7) offshore Kythira Island, southern Greece: seismological, strong-motion, and macroseismic observations of an intermediate-depth event, *Seismol. Res. Lett.,* **77**(5), 544–553.

Kontogianni, V.A., Tsoulos, N. & Stiros, S.C., 2002. Coastal uplift, earthquakes and active faulting of Rhodes Island (Aegean Arc): modeling based on geodetic inversion, *Mar. Geol.,* **186**(3–4), 299–317.

Kositsky, A.P. & Avouac, J.-P., 2010. Inverting geodetic time series with a principal component analysis-based inversion method, *J. geophys. Res.,* **115**(B3), B03401, doi:10.1029/2009JB006535.

Lay, T., 2015. The surge of great earthquakes from 2004 to 2014, *Earth planet. Sci. Lett.,* **409,** 133–146.

Lay, T., Ammon, C.J., Kanamori, H., Rivera, L., Koper, K.D. & Hutko, A.R., 2010. The 2009 Samoa-Tonga great earthquake triggered doublet, *Nature,* **466**(7309), 964–968.

Le Pichon, X. *et al.*, 1979. From subduction to transform motion: a seabeam survey of the Hellenic trench system, *Earth planet. Sci. Lett.,* **44**(3), 441–450.

Louvari, E., Kiratzi, A. & Papazachos, B., 1999. The Cephalonia Transform Fault and its extension to western Lefkada Island (Greece), *Tectonophysics,* **308**(1), 223–236.

Loveless, J.P., Hoke, G.D., Allmendinger, R.W., González, G., Isacks, B.L. & Carrizo, D.A., 2005. Pervasive cracking of the northern Chilean Coastal Cordillera: new evidence for forearc extension, *Geology,* **33**(12), doi:10.1130/G22004.1.

Lyon-Caen, H. *et al.*, 1988. The 1986 Kalamata (South Peloponnesus) Earthquake: detailed study of a normal fault, evidences for east-west extension in the Hellenic Arc, *J. geophys. Res.,* **93**(B12), 14 967–15 000.

Maggi, A., Jackson, J.A., Priestley, K. & Baker, C., 2000. A re-assessment of focal depth distributions in southern Iran, the Tien Shan and northern India: do earthquakes really occur in the continental mantle?, *Geophys. J. Int.,* **143**(3), 629–661.

Mahsas, A., Lammali, K., Yelles, K., Calais, E., Freed, A.M. & Briole, P., 2008. Shallow afterslip following the 2003 May 21, M_W 6.9 Boumerdes earthquake, Algeria, *Geophys. J. Int.,* **172**(1), 155–166.

Makris, J., Papoulia, J. & Yegorova, T., 2013. A 3-D density model of Greece constrained by gravity and seismic data, *Geophys. J. Int.,* **194**(1), 1–17.

Mascle, J. & Le Quellec, P., 1980. Matapan trench (Ionian Sea): example of trench disorganization?, *Geology,* **8**(2), doi:10.1130/0091-7613(1980)8⟨77:MTISEO⟩2.0.CO;2.

Mason, J., Reicherter, K. & Papanikolaou, I., 2015. The Lapithas Mountain faults and nearby archaeological damage, western Peloponnese, Greece, *Z. Geomorphol. Suppl. Issues,* **59**(4), 189–213.

McCaffrey, R. & Abers, G., 1988. SYN3: a program for inversion of Teleseismic body wave forms on microcomputers, Southeastern Center for Electrical Engineering Education Inc., St. Cloud, FL.

McCaffrey, R., Zwick, P. & Abers, G., 1991. SYN4 program, *IASPEI Softw. Libr.,* **3,** 81–166.

McKenzie, D., 1978. Active tectonics of the Alpine–Himalayan belt: the Aegean Sea and surrounding regions, *Geophys. J. R. astr. Soc.,* **55,** 217–254.

McNeill, L. & Collier, R., 2004. Uplift and slip rates of the eastern Eliki fault segment, Gulf of Corinth, Greece, inferred from Holocene and Pleistocene terraces, *J. Geol. Soc. Lond.,* **161**(1), 81–92.

Meier, T., Rische, M., Endrun, B., Vafidis, A. & Harjes, H.P., 2004. Seismicity of the Hellenic subduction zone in the area of western and central Crete observed by temporary local seismic networks, *Tectonophysics,* **383**(3), 149–169.

Melnick, D., 2016. Rise of the central Andean coast by earthquakes straddling the Moho, *Nat. Geosci.,* **9** (March), 1–8.

Molnar, P. & Lyon-Caen, H., 1989. Fault plane solutions of earthquakes and active tectonics of the Tibetan Plateau and its margins, *Geophys. J. Int.,* **99**(1), 123–154.

Mouslopoulou, V., Begg, J., Nicol, A., Oncken, O. & Prior, C., 2015. Formation of Late Quaternary paleoshorelines in Crete, Eastern Mediterranean, *Earth planet. Sci. Lett.,* **431,** 294–307.

Nocquet, J.-M., 2012. Present-day kinematics of the Mediterranean: a comprehensive overview of GPS results, *Tectonophysics,* **579,** 220–242.

Noda, H. & Lapusta, N., 2013. Stable creeping fault segments can become destructive as a result of dynamic weakening, *Nature,* **493**(7433), 518–521.

Okada, Y., 1985. Surface deformation due to shear and tensile faults in a half-space, *Bull. seism. Soc. Am.,* **75**(4), 1135–1154.

Ozawa, S., Nishimura, T., Suito, H., Kobayashi, T., Tobita, M. & Imakiire, T., 2011. Coseismic and postseismic slip of the 2011 magnitude-9 Tohoku-Oki earthquake, *Nature,* **475**(7356), 373–376.

Papadimitriou, E.E. & Karakostas, V.G., 2008. Rupture model of the great AD 365 Crete earthquake in the southwestern part of the Hellenic Arc, *Acta Geophys.,* **56**(2), 293–312.

Papanikolaou, D., Fountoulis, I. & Metaxas, C., 2007. Active faults, deformation rates and Quaternary paleogeography at Kyparissiakos Gulf (SW Greece) deduced from onshore and offshore data, *Quat. Int.,* **171-172** (SPEC. ISS.), 14–30.

Papoulia, J. & Makris, J., 2004. Microseismicity and active deformation of Messinia, SW Greece, *J. Seismol.,* **8**(4), 439–451.

Pearce, F.D., Rondenay, S., Sachpazi, M., Charalampakis, M. & Royden, L.H., 2012. Seismic investigation of the transition from continental to oceanic subduction along the western Hellenic Subduction Zone, *J. geophys. Res.,* **117**(B7), B07306, doi:10.1029/2011JB009023.

Perfettini, H., Avouac, J.-P. & Ruegg, J.-C., 2005. Geodetic displacements and aftershocks following the 2001 $M_W = 8.4$ Peru earthquake: implications for the mechanics of the earthquake cycle along subduction zones, *J. geophys. Res.,* **110**(B9), doi:10.1029/2004JB003522.

Peters, J.M., Troelstra, S.R. & van Harten, D., 1985. Late Neogene and Quaternary vertical movements in eastern Crete and their regional significance, *J. Geol. Soc. Lond.,* **142**(3), 501–513.

Pirazzoli, P., Thommeret, J., Thommeret, Y., Laborel, J. & Montaggioni, L., 1982. Crustal block movements from Holocene shorelines: Crete and Antikythira (Greece), *Tectonophysics,* **86**(1–3), 27–43.

Pirazzoli, P.A., Montaggioni, L.F., Saliege, J.F., Segonzac, G., Thommeret, Y. & Vergnaud-Grazzini, C., 1989. Crustal block movements from Holocene shorelines: Rhodes island (Greece), *Tectonophysics,* **170**(1–2), 89–114.

Pirazzoli, P.A., Laborel, J. & Stiros, S.C., 1996. Earthquake clustering in the eastern Mediterranean during historical times, *J. geophys. Res.,* **101**(B3), 6083–6097.

Reilinger, R. *et al.*, 2006. GPS constraints on continental deformation in the Africa-Arabia-Eurasia continental collision zone and implications for the dynamics of plate interactions, *J. geophys. Res.,* **111**(B5), B05411, doi:10.1029/2005JB004051.

Roumelioti, Z., Benetatos, C. & Kiratzi, A., 2009. The 14 February 2008 earthquake (M6.7) sequence offshore south Peloponnese (Greece): source models of the three strongest events, *Tectonophysics,* **471**(3–4), 272–284.

Sachpazi, M. *et al.*, 2015. Segmented Hellenic slab rollback driving Aegean deformation and seismicity, *Geophys. Res. Lett.,* **43,** 651–658.

Sandwell, D.T., Müller, R.D., Smith, W., Garcia, H.F.E. & Francis, R., 2014. Marine geophysics. New global marine gravity model from CryoSat-2 and Jason-1 reveals buried tectonic structure, *Science,* **346**(6205), 65–67.

Schmid, R., Steigenberger, P., Gendt, G., Ge, M. & Rothacher, M., 2007. Generation of a consistent absolute phase-center correction model for GPS receiver and satellite antennas, *J. Geod.,* **81**(12), 781–798.

Scholz, C.H., Aviles, C.A. & Wesnousky, S.G., 1986. Scaling differences between large interplate and intraplate earthquakes, *Bull. seism. Soc. Am.,* **76**(1), 65–70.

Serpetsidaki, A. *et al.*, 2014. New constraints from seismology and geodesy on the $M_W = 6.4$, 2008 Movri (Greece) earthquake: evidence for a growing strike-slip fault system, *Geophys. J. Int.,* **198**(3), 1373–1386.

Shaw, B. & Jackson, J., 2010. Earthquake mechanisms and active tectonics of the Hellenic subduction zone, *Geophys. J. Int.,* **181,** 966–984.

Shaw, B. *et al.*, 2008. Eastern Mediterranean tectonics and tsunami hazard inferred from the AD 365 earthquake, *Nat. Geosci.,* **1**(4), 268–276.

Siebert, L. & Simkin, T., 2002. Volcanoes of the World: an illustrated catalog of Holocene volcanoes and their eruptions, Smithsonian Institution Digital Information Series GVP-3. Available at: http://www.volcano.si.edu/gvp/world.

Spratt, T.A.B., 1865. *Travels and Researches in Crete,* vols I and II, J. van Voorst.

Stiros, S., Moschas, F., Feng, L. & Newman, A., 2013. Long-term versus short-term deformation of the meizoseismal area of the 2008 Achaia–Elia (M_W 6.4) earthquake in NW Peloponnese, Greece: evidence from historical triangulation and morphotectonic data, *Tectonophysics,* **592,** 150–158.

Stiros, S.C., 2010. The 8.5+ magnitude, AD365 earthquake in Crete: Coastal uplift, topography changes, archaeological and historical signature, *Quat. Int.,* **216**(1–2), 54–63.

Stiros, S.C. & Drakos, A., 2006. A fault model for the tsunami-associated, magnitude $\geq$ 8.5 eastern Mediterranean, AD 365 earthquake, *Z. Geomorphol. Suppl. Issues,* **146,** 125–137.

Stiros, S.C., Laborel, J., Laborel-Deguen, F., Papageorgiou, S., Evin, J. & Pirazzoli, P.A., 2000. Seismic coastal uplift in a region of subsidence: Holocene raised shorelines of Samos Island, Aegean Sea, Greece, *Mar. Geol.,* **170,** 41–58.

Strobl, M., Hetzel, R., Fassoulas, C. & Kubik, P., 2014. A long-term rock uplift rate for eastern Crete and geodynamic implications for the Hellenic subduction zone, *J. Geodyn.,* **78,** 21–31.

Tarantola, A., 2005. *Inverse Problem Theory and Methods for Model Parameter Estimation,* Society for Industrial and Applied Mathematics.

Taymaz, T., Jackson, J. & Westaway, R., 1990. Earthquake mechanisms in the Hellenic Trench near Crete, *Geophys. J. Int.,* **102**(3), 695–731.

Taymaz, T., Jackson, J. & McKenzie, D., 1991. Active tectonics of the north and central Aegean Sea, *Geophys. J. Int.,* **106**(2), 433–490.

Thomas, M.Y., Avouac, J.-P., Champenois, J., Lee, J.-C. & Kuo, L.-C., 2014. Spatiotemporal evolution of seismic and aseismic slip on the Longitudinal Valley Fault, Taiwan, *J. geophys. Res.,* **119**(6), 5114–5139.

Tregoning, P. & van Dam, T., 2005. Atmospheric pressure loading corrections applied to GPS data at the observation level, *Geophys. Res. Lett.,* **32**(22), doi:10.1029/2005GL024104.

Tsuji, T., Kawamura, K., Kanamatsu, T., Kasaya, T., Fujikura, K., Ito, Y., Tsuru, T. & Kinoshita, M., 2013. Extension of continental crust by anelastic deformation during the 2011 Tohoku-oki earthquake: the role of extensional faulting in the generation of a great tsunami, *Earth planet. Sci. Lett.,* **364,** 44–58.

Vernant, P., Reilinger, R. & McClusky, S., 2014. Geodetic evidence for low coupling on the Hellenic subduction plate interface, *Earth planet. Sci. Lett.,* **385,** 122–129.

Vigny, C. *et al.*, 2011. The 2010 M_W 8.8 Maule megathrust earthquake of Central Chile, monitored by GPS, *Science,* **332**(6036), 1417–1421.

Vitard, C., 2015. Structural analysis of the southwestern segment of the Hellenic subduction zone by joint analysis of seismic reflection and refraction, in *AGU Fall Meeting,* San Francisco.

Wegmann, K., 2008. Tectonic geomorphology above Mediterranean subduction zones, northern Apennines of Italy and Crete, Greece, *PhD thesis,* Lehigh University, Bethlehem, PA.

Wells, D.L. & Coppersmith, K.J., 1994. New empirical relationships among magnitude, rupture length, rupture width, rupture area, and surface displacement, *Bull. seism. Soc. Am.,* **84**(4), 974–1002.

Wessel, P., Smith, W.H.F., Scharroo, R., Luis, J. & Wobbe, F., 2013. Generic mapping tools: improved version released, *EOS, Trans. Am. geophys. Un.,* **94**(45), 409–420.

Wesson, R.L., Melnick, D., Cisternas, M., Moreno, M. & Ely, L.L., 2015. Vertical deformation through a complete seismic cycle at Isla Santa María, Chile, *Nat. Geosci.,* **8**(7), 547–551.

Williams, S.D.P., 2008. CATS: GPS coordinate time series analysis software, *GPS Solut.,* **12**(2), 147–153.

Zelilidis, A., Kontopoulos, N., Avramidis, P. & Piper, D., 1998. Tectonic and sedimentological evolution of the Pliocene–Quaternary basins of Zakynthos island, Greece: case study of the transition from compressional to extensional tectonics, *Basin Res.,* **10**(4), 393–408.

Zumberge, J.F., Heflin, M.B., Jefferson, D.C., Watkins, M.M. & Webb, F.H., 1997. Precise point positioning for the efficient and robust analysis of GPS data from large networks, *J. geophys. Res.,* **102**(B3), 5005–5017.

Zwick, P., McCaffrey, R. & Abers, G., 1994. MT5 program, *IASPEI Softw. Libr.,* **4**.

SUPPORTING INFORMATION

Supplementary data are available at *GJIRAS* online.

Figure S1. Fit of synthetic to observed waveforms for the 2013 October 12 M_W 6.5 earthquake.
Figure S2. Fit of modelled to observed post-seismic time series at station ATRS (Fig. 4, main text).
Figure S3. Fit of modelled to observed post-seismic time series at station KERY (Fig. 4, main text).
Figure S4. Fit of modelled to observed post-seismic time series at station KITH (Fig. 4, main text).
Figure S5. Fit of modelled to observed post-seismic time series at station METH (Fig. 4, main text).
Figure S6. Fit of modelled to observed post-seismic time series at station VASS (Fig. 4, main text).
Table S1. Uplift measurements used in the grid searches in Appendix B.

Please note: Oxford University Press is not responsible for the content or functionality of any supporting materials supplied by the authors. Any queries (other than missing material) should be directed to the corresponding author for the paper.

APPENDIX A: AFTERSLIP UNDER THE PELOPONNESE

In Section 4.4, we show results of a model for which the inversion is allowed to specify slip on the subduction interface up to a depth of 45 km (Fig. 7). The inversion specifies minimal slip for all of the patches NE of the coastline except four; we suggest that for these patches the inversion is fitting the noise in the time-series at individual stations (ATRS and KITH in particular). Fig. A1(a) shows the fit of the model to the data for an inversion where slip is specified to be shallower than 35 km. This model is able to fit the observed post-seismic offsets at our stations (Fig. A1b), so our GPS data are consistent with slip only in the region SW of the coastline.

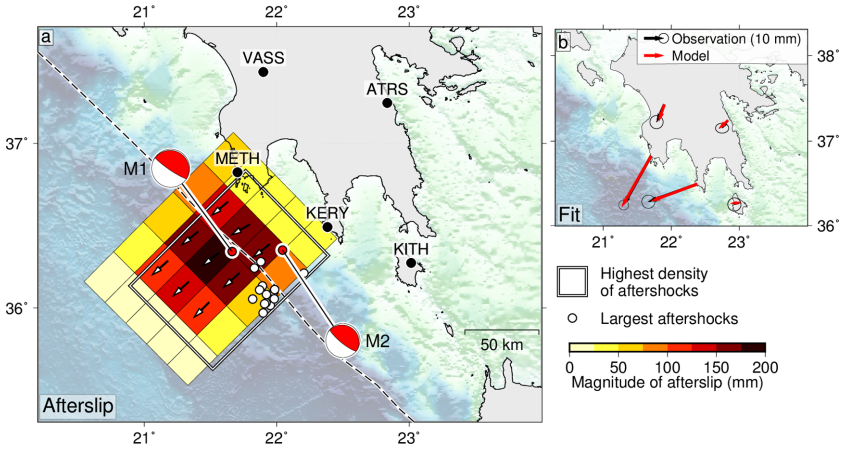

Figure A1. (a) Results of afterslip inversion using the PCAIM software of Kositsky & Avouac (2010). Slip was inverted for using one principal component and a value for the Laplacian smoothing operator of 10^3 and was restricted to be shallower than 35 km depth. The Methoni earthquakes (M1 and M2) are shown, the trace of the Hellenic Trench is shown by a dashed black line and the stations used in the inversion are shown by black circles. Arrows show slip-vector directions for fault patches where the inversion predicts mean slip ≥50 mm and the white box shows the region with the highest spatial density of aftershocks (see Fig. 8). (b) Fit of the model in (a) to cumulative displacements in the 3 yr following the Methoni earthquakes.

APPENDIX B: QUANTITATIVE TEST OF THE SUGGESTION THAT THE LATE-HOLOCENE UPLIFT OF SW CRETE IS ATTRIBUTABLE TO NORMAL FAULTING

B1 Background

Late-Holocene palæoshorelines are observed throughout SW Crete at elevations of up to 9 m above present-day mean sea level (e.g. Spratt 1865; Pirazzoli *et al.* 1982). Radiocarbon dates from marine fauna found between these palæoshorelines and present-day sea level show that this uplift occurred between 1500 and 2000 yr BP, plausibly during the earthquake of 21 July, AD 365 (e.g. Pirazzoli *et al.* 1996; Shaw *et al.* 2008; Stiros 2010). Calculation of the distortion of the earth's surface as a result of fault slip shows that the distribution of elevations of these shorelines is consistent with slip on a reverse fault cropping out near the Hellenic Trench (e.g. Stiros & Drakos 2006; Papadimitriou & Karakostas 2008; Shaw *et al.* 2008; Stiros 2010).

The uplift of Crete has also, however, been attributed to normal faulting. Wegmann (2008) suggested that the AD 365 earthquake occurred on a normal fault cropping out to the south of Crete and was responsible for the late-Holocene uplift of SW Crete, and Gallen *et al.* (2014) suggested that some of the trenches in the Hellenic Trench System are the bathymetric expression of normal faulting. The purpose of this appendix is to put that suggestion to a quantitative test. The only quantitative data available are the elevations of the Late-Holocene palæoshorelines and we analyse these using the standard techniques of elastic deformation modelling in order to determine what source parameters are required if a normal-faulting earthquake is to match the observed uplift.

We frame our discussion in terms of a single event, which we refer to for brevity as the AD 365 earthquake, because Shaw *et al.* (2008) showed that at least 7 m of the maximum 9 m of uplift occurred in AD 365, plus or minus the uncertainties of the radiocarbon data. The calculations are linear, so the Late-Holocene uplift may also be treated as the sum of multiple smaller slip events on the same fault, provided that the proposed events do not violate the radiocarbon data. Equally, the calculations may be used to assess the plausibility that Quaternary uplift of western Crete is attributable to long-term slip on the same configurations of fault.

B2 Modelling

We treat slip on the fault as a rectangular dislocation in an infinite elastic half-space, using the method of Okada (1985). Nine parameters are required to define the dislocation: the magnitude of the slip and its rake, the dip of the plane, the locations of the end-points of its surface projection, and the minimum and maximum depths of slip. We perform systematic grid searches through the last seven of these parameters. The distribution of uplift depends linearly on the strike-slip and dip-slip components of the slip, which we solve for by standard least-squares techniques.

We consider four categories of fault model (Fig. B1):

(A) A reverse fault with its surface projection in the Hellenic Trench escarpment, as proposed by Shaw *et al.* (2008).

(B) A normal fault that projects to the surface in the Hellenic Trench. If uplift of Crete in AD 365 did occur in the footwall of a normal fault, the Hellenic Trench is the most obvious bathymetric expression of slip on such a fault.

(C) A normal fault with the same strike as the Hellenic Trench that projects to the surface close to the coast of Crete. To our knowledge there is no evidence for a fault of this type either in bathymetric or reflection seismic data (e.g. Chaumillon & Mascle 1997; Kokinou & Kamberis 2009; Vitard 2015). We nevertheless consider such a fault because, if it were to exist, it would require a smaller ratio of slip to uplift than faults of category B; this model allows us to estimate the minimum slip required on a normal fault with the same strike as the Hellenic Trench (315°).

(D) A normal fault that projects to the surface in the S Cretan Trough, a bathymetric depression that runs ∼E–W along the S side of W Crete, reaching ∼1300 m depth. Gallen *et al.* (2014) interpreted this the eastern part of this trough as the expression of arc-perpendicular extension, consistent with the presence of arc-parallel normal faults on Crete (e.g. Caputo *et al.* 2010; Gallen *et al.* 2014).

In all our calculations, the dislocation representing the model fault intersects the surface; this minimizes the slip required to fit the distribution of uplift. We vary the maximum depth of rupture by 5 km increments between 20 and 45 km, which is the maximum depth of microseismicity on Crete and the approximate depth of the Eurasia–Nubia subduction interface beneath W Crete (this study and Shaw & Jackson 2010). As will be discussed, this lower limit restricts the length scale over which the uplift develops but normal faults dipping trenchwards to a greater depth would cut the downgoing plate. Each fault model is specified by a point on its intersection with the surface, and fault length is varied in 5 km increments between 30 and 200 km.

For Model A, we use the strike, dip, and rake given by Shaw *et al.* (2008) and allow the location of the surface projection of the fault to vary. We perform a grid search for the location of the fault surface projection, allowing it to vary in 5 km increments from a point in the Hellenic Trench, finding the locations of the fault end-points for which the RMS misfit between calculated and observed uplift at 29 sites on Crete, Gavdos and Antikythira is smallest. The best-fitting source parameters are listed in Table B1 and the uplift measurements are provided in the supplementary information.

We perform similar grid searches for models B, C and D. The strikes of fault models B and C are fixed at 135° (the strike of the Hellenic Trench) and the strike of model D is fixed at 110° (the strike of the S Cretan Trough close to W Crete). We set the rake of each model fault to be −90° (pure dip-slip) because: (1) the normal faults observed on Crete exhibit predominantly dip-slip behaviour (e.g. Caputo *et al.* 2010); (2) any strike-slip component of faulting would be poorly constrained by the observations of uplift; and (3) there is no evidence from seismicity, GPS or field data for significant strike-slip faulting in the overriding plate. We allow the dip of the faults to vary from 30° in steps of 5° to 75°, which is the steepest dip observed for a well-constrained normal-faulting earthquake with a known fault plane (Copley *et al.* 2012).

For model B, we constrain the centre of the surface projection of the fault to lie in the Hellenic Trench, allowing it to move along strike in 5 km increments. In the case of model C, we also allow the surface projection to move towards the coast in 5 km steps. The surface projection of model D is allowed to move both across-strike and along-strike in increments of 5 km from a point in the S Cretan Trough. The best-fitting source parameters and calculated values of M_W for models B, C and D are listed in Table B1.

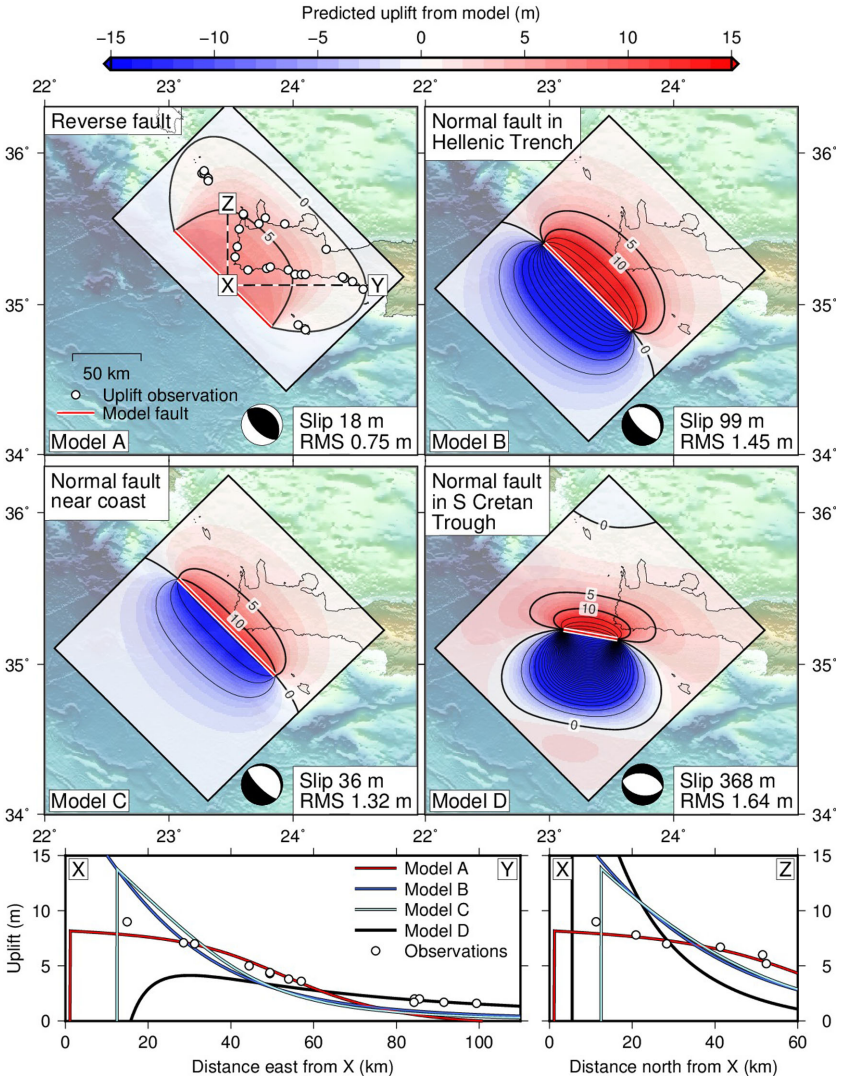

Figure B1. Results of grid searches for fault models that fit the observed late-Holocene uplift of SW Crete. Model A is the reverse-faulting model of Shaw *et al.* (2008). Model B is a normal-faulting source model for a fault that projects to the surface in the Hellenic Trench. Model C shows a normal fault with the same strike as the Hellenic Trench but a surface projection closer to the coast of Crete. Model C is a normal fault that projects to the surface in the SW Cretan Trough. The lower two panels show predicted uplift from the four models along the profiles X–Y and X–Z along the S and E coasts of Crete, with the uplift observed at localities along these coasts shown by white circles. Model fault surface projections are shown by red lines and focal mechanisms associated with each model are shown in black.

Table B1. Source parameters and moment magnitudes for the fault models in Fig. B1. M_W is calculated using the method of Hanks & Kanamori (1979). Longitude and latitude are for the centre of the surface projection of the fault. Max depth refers to the depth of the lower limit of slip in the fault model. Slip reaches the surface in all models. Root mean square (RMS) misfits between uplift predicted by the models and observed uplift at 29 sites on Crete are in the right-hand column.

Model	Longitude (°)	Latitude (°)	Strike (°)	Dip (°)	Rake (°)	Length (km)	Max depth (km)	Slip (m)	M_W	RMS (m)
A	23.435	35.169	315	30	90	100	45	18	8.4	0.75
B	23.310	35.118	135	70	−90	90	45	99	8.7	1.45
C	23.467	35.245	135	75	−90	100	45	36	8.5	1.32
D	23.330	35.198	100	45	−90	40	45	368	8.9	1.64

B3 Results

Fig. B1 shows the best-fitting fault models from each of our four grid searches. The lower panels show the fits of the models to observed uplift on the S and W coasts of Crete. These panels and the calculated RMS misfit show that none of the normal-faulting models that we have considered fits the observed uplift as well as the reverse-faulting model in A.

The minimum slip required on the normal faults is the 36 m for Model C, the normal fault nearest to the south coast of Crete. This comfortably exceeds the highest magnitude of slip for a normal-faulting earthquake during the instrumental seismological era [~10 m during the 2009 Samoa–Tonga earthquake (Lay *et al.* 2010)]. Recall that this model, for which there is no bathymetric or reflection-seismic evidence, was chosen specifically to allow the minimum ratio of slip to uplift. The slip required for Models B

and D are, respectively ∼100 m and ∼370 m. These magnitudes of slip correspond to moment magnitudes (M_W) of 8.7 and 8.9 respectively and ratios of slip to length of 10^{-3} and 10^{-2}, which greatly exceed the ratios calculated by Scholz *et al.* (1986) and Wells & Coppersmith (1994), which are typically 10^{-5} to 10^{-4}.

Furthermore, Models B, C, and D exhibit systematic misfits to the data, with too much uplift near the fault, and too little uplift far from the fault (lower panels Fig. B1). All of the best-fitting models require that slip goes to the maximum depth (45 km) permitted in the grid searches. This systematic misfit may be reduced by allowing slip to continue to greater depth, thus permitting uplift further north and east on Crete, but seismological data show that the subduction interface is at ∼45 km beneath Crete. Normal faults that ruptured to greater than this depth would cut the subducting slab, which seems improbable.

We therefore conclude that the observed distribution of late-Holocene uplift of SW Crete is inconsistent with footwall uplift during a normal-faulting earthquake. Unrealistically large slip is required to match the 9 m of uplift observed in the very SW of Crete and even normal-faulting models that rupture to 45 km do not predict uplift on a wavelength long enough to be consistent with uplift observations.